Nonperturbative approach to Casimir interactions in periodic geometries

Rauno Büscher and Thorsten Emig

Institut für Theoretische Physik, Universität zu Köln, Zülpicher Straße 77, 50937 Köln, Germany
(Received 26 January 2004; published 2 June 2004)

Due to their collective nature Casimir forces can strongly depend on the geometrical shape of the interacting objects. We study the effect of *strong* periodic shape deformations of two ideal metal plates on their quantum interaction. A nonperturbative approach which is based on a path-integral quantization of the electromagnetic field is presented in detail. Using this approach, we compute the force for the specific case of a flat plate and a plate with a rectangular corrugation. We obtain complementary analytical and numerical results which allow us to identify two different scaling regimes for the force as a function of the mean plate distance, corrugation amplitude, and wavelength. Qualitative distinctions between transversal electric and magnetic modes are revealed. Our results demonstrate the importance of a careful consideration of the nonadditivity of Casimir forces, especially in strongly nonplanar geometries. Nonperturbative effects due to surface edges are found. Strong deviations from the commonly used proximity force approximation emerge over a wide range of corrugation wavelengths, even though the surface is composed only of flat segments. We compare our results to that of a perturbative approach and a classical optics approximation.

I. INTRODUCTION

Casimir interactions [1–5] are a fundamental property of the vacuum. They are commonly related to quantum electrodynamics but fluctuation-induced interactions are of interest in a wide variety of other fields like in condensed-matter systems such as liquid crystals and superfluids [6,7], in cosmological models [8], in particle physics [9,10], and in biological systems such as proteins on membranes. The guiding mechanism behind all these phenomena is that a quantum or thermal field is constrained by boundary conditions on surfaces so that the energy is modified, and effective interactions between the surfaces occur. For quantum fields the Casimir interaction is given by the *change* in the ground-state energy $\mathcal{E}_0 = \frac{1}{2}\Sigma_n \hbar\omega_n$ due to the presence of boundary conditions. Even for noninteracting fields like the photon gauge field it is difficult to obtain the Casimir interaction since the eigenfrequencies ω_n can depend strongly on the confining geometry. Thus it is not unexpected that exact analytical results for Casimir interactions between macroscopic objects are not known even if the geometry has high symmetry.

Most of the recent high-precision experiments aim at the measurement of the Casimir force in geometries which are closely related to the standard case of two parallel plates [11–14]. To the latter case applies Casimir's seminal prediction [1]

$$\frac{F_{\text{flat}}}{A} = -\frac{\pi^2}{240}\frac{\hbar c}{H^4} \qquad (1)$$

for the force between two ideal metallic and parallel plane plates of area A and distance H at zero temperature. For technical reasons, usually a plate-sphere geometry is used in experiments. Even for this case only approximative methods such as the proximity force or Derjaguin approximation [15] can be applied and the exact result is not known. There exists geometries for which there is even little intuition as to whether the interaction is attractive or repulsive. A striking

example is Boyer's result that the Casimir energy of a conducting sphere is *positive* [16]. This observation has triggered a search for repulsive configurations [17,18]. Such effects can be even of direct practical relevance in nanotechnology where "sticking" of mobile components in micromachines might be caused by Casimir forces [19].

The advances in experimental techniques have stimulated the measurement of the shape dependence of Casimir forces in specially designed geometries (as opposed to inevitable geometrical effects such as surface roughness). Mohideen and co-workers were able to measure the Casimir force between a sphere of large curvature radius and a corrugated plate [20,21]. Although the corrugation length was larger than the studied range of separations between the surfaces, their results showed a clear deviation from predictions of the proximity force approximation. While it has been suggested [22] that lateral surface displacements caused this discrepancy, there is no reason to believe in the validity of the proximity approximation if the corrugation length is decreased.

Because of the wide range of realizations of Casimir forces, improved experimental techniques, and the increasing importance of nanostructures, it is interesting to develop approaches for computing such interactions. In the limit of slight surface deformations a path-integral quantization subject to boundary conditions allows for a perturbative calculation of the interaction [23,24], showing strong corrections to the proximity approximation [25,26]. Another perturbative approach, based on a multiple-scattering expansion, has been applied to the limit of large surface separations [27]. Very recently, an alternative approximation scheme based on geometric optics has been proposed for geometries where the Casimir interaction is mostly caused by short wavelengths [28]. A characterization of Casimir interactions between spherical conductors in terms of classical optics properties of the geometry was also obtained within a semiclassical treatment [29]. However, to date no systematic method is known for estimating interactions of strongly deformed objects, in-

cluding large curvature or even sharp edges. In this paper we present a nonperturbative method to compute electrodynamic Casimir interactions between uniaxially and periodically deformed surfaces. It is based on a path-integral approach for Casimir forces [30,31]. The approach is not restricted to small deformations or small surface curvature but it also allows us to study strong deformations and edges. We develop a numerical implementation of the approach which allows for a precise computation of the interaction without any approximations. As an example we consider a geometry consisting of a flat and a rectangular corrugated plate, see Fig. 2. For this geometry we obtain the Casimir force over a wide range of surface separations and corrugation lengths. We find that the edges of the corrugated surface cause strong deviations from the proximity approximation, which agrees reasonably with our results only if the corrugation length is much larger than both the surface distance and the corrugation amplitude. We show that the qualitative effect of edges on the interaction can be understood in the limit of large corrugation lengths in terms of classical ray optics. A brief account of our method and its application to scalar fields subject to Dirichlet boundary conditions appeared in Ref. [32].

The rest of this work is organized as follows. In Sec. II we review briefly the path-integral approach and then introduce the method for a nonperturbative computation of Casimir interactions. We consider periodic uniaxially deformed surfaces. The approach is then applied in Sec. III to the example of a flat and a corrugated surface with sharp edges. The asymptotic limits of small and large corrugation lengths are treated analytically. For arbitrary corrugation lengths the interaction is obtain by a numerical implementation of our approach. We give detailed numerical results for the total electromagnetic Casimir force and the contributions from TM and TE modes separately. In Sec. IV we compare our results to perturbation theory for slightly deformed smooth surfaces. We interpret our results for large corrugation length in terms of classical ray optics. Throughout the paper we set $c=1$ and $\hbar=1$.

II. NONPERTURBATIVE PATH-INTEGRAL APPROACH

We consider two perfectly conducting periodically deformed (corrugated) plates S_α ($\alpha=1,2$) with a mean separation H. They are assumed to be infinitely extended over a base plane which is parametrized by the coordinates $\mathbf{x}_\parallel = (x_1, x_2)$. For simplicity we assume that the corrugation is uniaxial along the x_1 direction. The shape of the plates is then described by height functions $h_\alpha(x_1)$ which measure deviations from the mean height so that $\int_{x_1} h_\alpha(x_1)=0$. The Casimir energy of the two plate configuration can be obtained from an imaginary time path integral representation [23,24] for the partition function of the electromagnetic field and the confining plates. In the absence of boundaries, the path integral extends over the electromagnetic gauge field A_μ with the four-dimensional (4D) space-time action

$$S_0[A^\mu] = -\frac{1}{4} \int d^4X \, F_{\mu\nu}F^{\mu\nu} \qquad (2)$$

and the field $F_{\mu\nu}=\partial_\mu A_\nu - \partial_\nu A_\mu$ and $X=(x_0,\mathbf{x}_\parallel,x_3)$. In order to eliminate redundant gauge-field configurations the Fadeev

Popov gauge fixing procedure has to be applied [33]. The ideal metal boundary condition for the gauge field $A_\mu(X)$ is given by the requirement that the tangential components of the electric field vanishes at the surfaces.

For plate deformations which are uniaxial, the translational invariant direction can serve as reference axis for defining TM and TE modes, similar to the treatment of wave guide geometries [34]. Then every field configuration can be decomposed into those two types of modes, and one can resort to a scalar field path-integral quantization [25,26]. The scalar fields are given by the electric- and magnetic-field components along the translational symmetry axis,

$$\Phi(X) = E_2(X) \quad \text{for TM modes,} \qquad (3)$$

$$\Phi(X) = B_2(X) \quad \text{for TE modes.} \qquad (4)$$

Since the plates are assumed to be ideally conducting, the boundary conditions for TM and TE modes are of Dirichlet and Neumann type, respectively; i.e.,

$$\Phi|_{S_\alpha} = 0 \quad \text{for TM modes,} \qquad (5)$$

$$\partial_{\hat{\mathbf{n}}_\alpha}\Phi|_{S_\alpha} = 0 \quad \text{for TE modes,} \qquad (6)$$

with the surface normal derivative denoted by $\partial_{\hat{\mathbf{n}}}$ pointing into the vacuum between the plates. After a Wick rotation to imaginary time $x_0 \to ix_0$, both types of modes are described by the Euclidean action

$$S_E\{\Phi\} = \frac{1}{2} \int d^4X \, (\nabla\Phi)^2. \qquad (7)$$

In 4D Euclidean space, the surface positions of the plates are then parametrized by $X_\alpha(\mathbf{r})=[\mathbf{r}, h_\alpha(x_1)+H\delta_{\alpha2}]$ with $\mathbf{r} \equiv (x_0, \mathbf{x}_\parallel)$. Following the procedure introduced in Refs. [30,31], the boundary conditions are imposed by inserting δ functions on the surface in the functional integral. The partition function for TM and TE modes, respectively, then reads

$$\mathcal{Z}_D = \mathcal{Z}_0^{-1} \int \mathcal{D}\Phi \prod_{\alpha=1}^{2} \prod_{X_\alpha} \delta(\Phi(X_\alpha)) e^{-S_E\{\Phi\}}, \qquad (8)$$

$$\mathcal{Z}_N = \mathcal{Z}_0^{-1} \int \mathcal{D}\Phi \prod_{\alpha=1}^{2} \prod_{X_\alpha} \delta(\partial_{\hat{\mathbf{n}}_\alpha}\Phi(X_\alpha)) e^{-S_E\{\Phi\}}, \qquad (9)$$

with the boundary free partition function $\mathcal{Z}_0$. The functional integrals can be calculated by introducing auxiliary fields to represent the δ functions. Then, the Gaussian integration over Φ can be carried out, yielding the partition function in terms of an effective action for the auxiliary fields,

$$\mathcal{Z} = \int \prod_{\alpha=1}^{2} \mathcal{D}\psi_\alpha \, e^{-S_{\text{eff}}\{\psi_\alpha\}}, \qquad (10)$$

with the effective action

$$S_{\text{eff}}\{\psi_\alpha\} = \frac{1}{2}\int_{\mathbf{r}}\int_{\mathbf{r}'}\sum_{\alpha,\beta}\psi_\alpha(\mathbf{r})\mathcal{M}^{\alpha\beta}(\mathbf{r};\mathbf{r}')\psi_\beta(\mathbf{r}'). \quad (11)$$

In the following we will drop the subscript D or N for the boundary conditions on all quantities, which apply to both conditions in the same way. The total electrodynamic Casimir energy is then given by the sum of TM and TE mode contributions, $\mathcal{E}=\mathcal{E}_{\text{TM}}+\mathcal{E}_{\text{TE}}$. After subtracting the divergent and H-independent terms, the energies can be written as $\mathcal{E}_{\text{TM}}=\ln\det(\mathcal{M}_D\mathcal{M}_{D,\infty}^{-1})/(2AL)$, and analogous to $\mathcal{E}_{\text{TE}}$ with D replaced by N, where $\mathcal{M}_{D,\infty}$ is the asymptotic expression of $\mathcal{M}_D$ for $H\rightarrow\infty$, A is the surface area of the plates, and L is the Euclidean length in time direction. The Casimir force $F=-\partial_H\mathcal{E}$ per unit area is then given by $F=F_{\text{TM}}+F_{\text{TE}}$, with

$$F_{\text{TM}} = -\frac{1}{2AL}\text{Tr}(\mathcal{M}_D^{-1}\partial_H\mathcal{M}_D), \quad (12a)$$

$$F_{\text{TE}} = -\frac{1}{2AL}\text{Tr}(\mathcal{M}_N^{-1}\partial_H\mathcal{M}_N). \quad (12b)$$

The right-hand side of these expressions is always finite, and no regulation of divergences by subtraction of the vacuum energy in the absence of boundaries is necessary. The Dirichlet and Neumann matrix kernels of the effective Gaussian action can be expressed in terms of the Euclidean scalar Green's function $\mathcal{G}(\mathbf{r},x_3)=(\mathbf{r}^2+x_3^2)^{-1}/(4\pi^2)$, and are respectively given by

$$\mathcal{M}_D^{\alpha\beta}(\mathbf{r};\mathbf{r}') = \eta_\alpha(x_1)\eta_\beta(x_1')\mathcal{G}(X_\alpha(\mathbf{r})-X_\beta(\mathbf{r}')), \quad (13a)$$

$$\mathcal{M}_N^{\alpha\beta}(\mathbf{r};\mathbf{r}') = \eta_\alpha(x_1)\eta_\beta(x_1')\partial_{\hat{\mathbf{n}}_\alpha(x_1)}\partial_{\hat{\mathbf{n}}_\beta(x_1')}\mathcal{G}(X_\alpha(\mathbf{r})-X_\beta(\mathbf{r}')), \quad (13b)$$

with the coefficients given by $\eta_\alpha(x_1)=(1+[(\partial_{x_1}h_\alpha)(x_1)]^2)^{1/4}$. These coefficients arise from the integral measure on the curved surfaces. However, since they are independent of the mean plate distance H, they cancel in the matrix product of Eq. (12) and therefore can be ignored for the calculation of forces. The kernels are symmetric with $\mathcal{M}(\mathbf{r};\mathbf{r}')=\mathcal{M}^{\text{T}}(\mathbf{r}';\mathbf{r})$, where the transpose refers to α, β. Using the parametrization in terms of height profiles, the matrix kernels can now be written as

$$\mathcal{M}_D^{\alpha\beta}(\mathbf{r};\mathbf{r}') = \mathcal{G}(\mathbf{r}-\mathbf{r}',h_\alpha(x_1)-h_\beta(x_1')+H(\delta_{\alpha2}-\delta_{\beta2})), \quad (14a)$$

$$\mathcal{M}_N^{\alpha\beta}(\mathbf{r};\mathbf{r}') = (-1)^{\alpha+\beta}\{-\partial_{x_3}^2+[h_\alpha'(x_1)+h_\beta'(x_1')]\partial_{x_1}\partial_{x_3}$$
$$-h_\alpha'(x_1)h_\beta'(x_1')\partial_{x_1}^2\}$$
$$\times\mathcal{G}(\mathbf{r}-\mathbf{r}',x_3-x_3')|_{x_3=h_\alpha(x_1)+H\delta_{\alpha2}} \quad (14b)$$
$$\qquad\qquad x_3'=h_\beta(x_1')+H\delta_{\beta2}$$

for the Dirichlet and Neumann case, respectively. So far, we have not used the periodicity of the surface profile, and the above results are valid for any uniaxial deformation. However, the computation of the force can be performed more

efficiently if the periodic symmetry of the surface is used.

Due to the translational invariance in time (x_0) and one space (x_2) direction, it is convenient to introduce the momentum vector $\mathbf{q}_\perp=(q_0,q_2)$ which is perpendicular to the direction of modulation. Due to the periodicity of the surface profile, the Fourier transform $\widetilde{\mathcal{M}}(\mathbf{p};\mathbf{q})=\int_{\mathbf{r}}\int_{\mathbf{r}'}e^{i\mathbf{p}\cdot\mathbf{r}+i\mathbf{q}\cdot\mathbf{r}'}\mathcal{M}(\mathbf{r};\mathbf{r}')$ can be decomposed into the series

$$\widetilde{\mathcal{M}}(p_1,\mathbf{p}_\perp;q_1,\mathbf{q}_\perp) = (2\pi)^3\delta(\mathbf{p}_\perp+\mathbf{q}_\perp)$$
$$\times\sum_{m=-\infty}^{\infty}\delta(p_1+q_1+2\pi m/\lambda)N_m(q_\perp,q_1), \quad (15)$$

where $N_m(q_\perp,q_1)$ are 2×2 matrices which depend only on $q_\perp=|\mathbf{q}_\perp|$. From Eq. (15) it is obvious that the matrix $\widetilde{\mathcal{M}}$ has its nonzero entries arranged in 2×2 blocks along parallel bands. Due to this structure, there exists a transformation, consisting only of row and column permutations, which makes the matrix block diagonal. To perform this transformation, we cut the matrix $\widetilde{\mathcal{M}}$ into smaller matrices $\mathcal{B}_{kl}$ which have nonzero entries only in 2×2 blocks along the diagonal, see Fig. 1. For the purpose of parametrization, we consider discrete momenta $q_1=(2\pi/W)j$, $j=0,\ldots,N$, along the direction of surface modulation with $N=W/\lambda-1$. The continuum limit is obtained if the linear size W of the surfaces and N are taken to infinity in order to obtain the force per unit surface area $A=W^2$. With this parametrization, the block-diagonal matrices $\mathcal{B}_{kl}$ of dimension $2(N+1)\times2(N+1)$ can be read off from Eq. (15), leading to

$$\mathcal{B}_{kl}(q_\perp)$$
$$= \text{diag}\{B_{kl}(q_\perp,0),B_{kl}(q_\perp,2\pi/W),\ldots,B_{kl}(q_\perp,2\pi N/W)\}, \quad (16)$$

with the 2×2 block matrices defined as (see Fig. 1)

$$B_{kl}(q_\perp,q_1) = N_{k-l}(q_\perp,q_1+2\pi l/\lambda). \quad (17)$$

By inspection of Fig. 1 one easily realizes that a sequence of row permutations and a subsequent sequence of column permutations transforms the matrix $\widetilde{\mathcal{M}}$ to block-diagonal form. Each of the $N+1$ blocks $\widetilde{\mathcal{M}}_j$ is composed of exactly one element from each matrix $\mathcal{B}_{kl}$ and those elements forming a block $\widetilde{\mathcal{M}}_j$ come from the same position in every matrix $\mathcal{B}_{kl}$ as indicated by the color scheme in Fig. 1. Thus, each block $\widetilde{\mathcal{M}}_j$ is composed of entries which correspond to the same discrete momentum $q_1=(2\pi/W)j$, and we obtain for the elements of $\widetilde{\mathcal{M}}_j$ the result

$$\widetilde{\mathcal{M}}_{j,kl}(\mathbf{p}_\perp,\mathbf{q}_\perp) = (2\pi)^2\ \delta(\mathbf{p}_\perp+\mathbf{q}_\perp)B_{kl}(q_\perp,2\pi j/W). \quad (18)$$

The number of permutations needed for the matrix transformation is always even, and thus we get the determinant
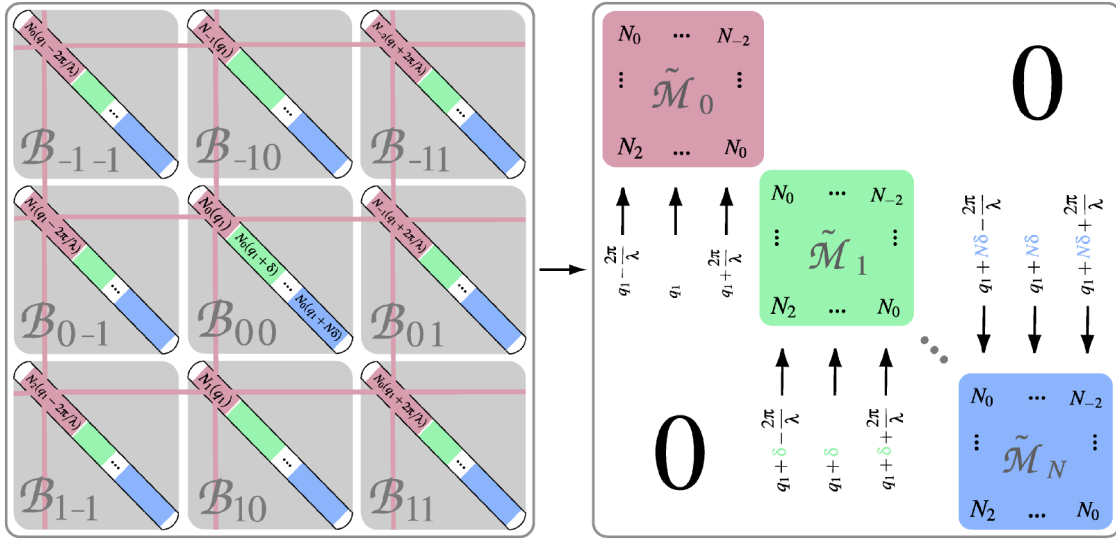
FIG. 1. (Color online) Transformation of the matrix $\tilde{\mathcal{M}}$ to block-diagonal form. The figure shows a finite part of the matrix, corresponding to the blocks $\mathcal{B}_{kl}$ with k, $l=-1,0,1$, before and after the permutations of rows and columns. Before the transformation (left box) $\tilde{\mathcal{M}}$ has a band structure with diagonal blocks $\mathcal{B}_{ij}$ consisting of 2×2 matrices N_m along the diagonal. (The dependence on the lateral momentum $\mathbf{q}_\perp$ is not shown here.) The first step of the transformation is to permute the rows and columns which are formed by the first entry N_m in every block $\mathcal{B}_{kl}$ (indicated as grid). These entries form after the permutations the first block $\tilde{\mathcal{M}}_0$ of $\tilde{\mathcal{M}}$ (right box). The latter permutation process is then repeated for the second and the third entry till the $(N+1)$th entry of every block $\mathcal{B}_{kl}$, leading to the $N+1$ blocks $\tilde{\mathcal{M}}_j$. The momenta q_1 within each block $\tilde{\mathcal{M}}_j$ are constant for every column and they differ only by integer multiples of $2\pi/\lambda$ between columns (of the same block), see labels in the right box. The blocks $\tilde{\mathcal{M}}_j$ differ in their momentum shift $j\delta$, $\delta=2\pi/W$, which is located in the unit cell $[0,2\pi/\lambda[$ since $j=0,\ldots,N=W/\lambda-1$.

$$\det\tilde{\mathcal{M}} = \prod_{j=0}^{N} \det\tilde{\mathcal{M}}_j. \tag{19}$$

By differentiating with respect to the mean surface distance H and by using the relation $\ln\det\tilde{\mathcal{M}}_j=\mathrm{Tr}\ln\tilde{\mathcal{M}}_j$, we obtain

$$\partial_H(\ln\det\tilde{\mathcal{M}}) = \sum_{j=0}^{N} \mathrm{Tr}(\tilde{\mathcal{M}}_j^{-1}\partial_H\tilde{\mathcal{M}}_j). \tag{20}$$

This result reflects the fact that the (free) energy of the system can be calculated as the sum of the individual (free) energies of *decoupled* subsystems, which are described by the matrices $\tilde{\mathcal{M}}_j$. Each subsystem with fixed j describes scattering events at the *fixed* momenta $q_1=(2\pi/W)j+(2\pi/\lambda)l$ which differ only by integer multiples of $2\pi/\lambda$.

Using Eq. (18) we can perform the trace over the continuous lateral momenta and the discrete indices within a fixed subsystem,

$$\mathrm{Tr}(\tilde{\mathcal{M}}_j^{-1} \cdot \partial_H\tilde{\mathcal{M}}_j) = \frac{LW}{(2\pi)^2}\int d^2\mathbf{q}_\perp \sum_{\substack{k,l=-\infty \\ \alpha,\beta=1,2}}^{\infty} B_{kl,\alpha\beta}^{-1}(q_\perp,2\pi j/W)$$

$$\times \partial_H B_{lk,\beta\alpha}(q_\perp,2\pi j/W), \tag{21}$$

where we have explicitly indicated that the trace is performed with respect to all discrete indices, and we remind that L is the system size in time direction. It appears useful to define the function

$$g(q_\perp,q_1) \equiv \mathrm{tr}[B^{-1}(q_\perp,q_1)\partial_H B(q_\perp,q_1)], \tag{22}$$

with the lower-case symbol tr denoting the trace over the discrete indices summed over in Eq. (21). Next we perform the sum over all subsystems with $j=0,\ldots,N=W/\lambda-1$. This can be easily done by going back to continuous momenta p_1. If we take the limit W, $N\to\infty$ with $W/(N+1)=\lambda$ fixed, the sum in Eq. (20) can be written as the integral

$$\partial_H(\ln\det\mathcal{M}) = \frac{LW}{(2\pi)^2}\int d^2\mathbf{q}_\perp \frac{W}{2\pi}\int_0^{2\pi/\lambda} dq_1 g(q_\perp,q_1). \tag{23}$$

The function $g(q_\perp,q_1)$ has the following symmetry properties. A shift of the momentum q_1 by $2\pi/\lambda$ corresponds just to a renumbering of the matrix elements B_{kl} since the matrix is of infinite dimension. Thus we have $g(q_\perp,q_1+2\pi/\lambda)=g(q_\perp,q_1)$. If both surface profiles are described by even functions, $h_\alpha(-x_1)=h_\alpha(x_1)$, for the matrices N_m the relation $N_m(q_\perp,-q_1)=N_{-m}(q_\perp,q_1)$ holds. Using the later relation and the definition of B_{kl} of Eq. (17) it is easy to check that $g(q_\perp,-q_1)=g(q_\perp,q_1)$ by performing appropriate row and column permutations for the matrix B. The above symmetries allow to write the Casimir force per unit area, $F/A=-(1/2LW^2)\partial_H(\ln\det\mathcal{M})$, as

$$F/A = -\frac{1}{4\pi^2} \int_0^\infty dq_\perp q_\perp \int_0^{\pi/\lambda} dq_1 \, g(q_\perp, q_1). \quad (24)$$

This is the final result of the general approach for arbitrary uniaxially corrugated surfaces. As we will show below, it can be used for an efficient numerical computation of the Casimir force. The input of such a numerical approach are the matrices N_m from the decomposition in Eq. (15). Moreover, the result can be also used to obtain nonperturbative analytical results in the asymptotic limit of very small corrugation lengths.

Before one can develop a numerical implementation of the above representation of the Casimir force, one of course has to restrict the infinite-dimensional matrices. In the remaining part of this section we will introduce a suitable cutoff procedure for the matrix dimension. We will take two flat plates as a simple example to examine the convergence of the procedure if the cutoff is taken to large values. The cutoff procedure consists in the restriction of the matrix $\widetilde{\mathcal{M}}$ to blocks $\mathcal{B}_{kl}$ with k, $l = -M, \dots, M$ only. The dimension of $\widetilde{\mathcal{M}}$ is then $2(2M+1)(N+1)$. Figure 1 displays the restricted matrix for $M = 1$. The corresponding function g is then defined by Eq. (22) with the restriction that the trace runs over k, $l = -M, \dots, M$ only. We will denote this function in the following by g_M. This function is then used instead of g in Eq. (24) to obtain a series of approximations F_M to the force which converges to F for $M \to \infty$. As an example consider two flat plates at distance H. Then $\widetilde{\mathcal{M}}$ is a diagonal matrix and $N_m = 0$ for $m \neq 0$. Thus the matrix B is also diagonal with

$$B_{kl}(q_\perp, q_1) = \delta_{kl} N_0(q_\perp, q_1 + 2\pi l/\lambda). \quad (25)$$

Using Eq. (22) with the trace taken for k, $l = -M, \dots, M$, one gets the function

$$g_M(q_\perp, q_1) = \sum_{l=-M}^{M} \frac{2\sqrt{q_\perp^2 + (q_1 + 2\pi l/\lambda)^2}}{e^{2\sqrt{q_\perp^2 + (q_1 + 2\pi l/\lambda)^2}H} - 1}. \quad (26)$$

Integration over q_1 yields an Mth-order approximation F_M to the force,

$$F_M/A = -\frac{1}{8\pi^2} \int_0^\infty dq_\perp q_\perp \int_0^{2\pi/\lambda} dq_1 g_M(q_\perp, q_1)$$

$$= -\frac{1}{8\pi^2} \int_0^\infty dq_\perp q_\perp \int_{-2\pi M/\lambda}^{2\pi(M+1)/\lambda} dq_1 \frac{2q}{e^{2qH} - 1}, \quad (27)$$

with $q = \sqrt{q_\perp^2 + q_1^2}$. For $M \to \infty$ one gets the known (λ-independent) result $F/A = -(\pi^2/480)H^{-4}$, and the finite M corrections to this asymptotic result scale exponentially fast ($\sim e^{-4\pi MH/\lambda}$) to zero for large M. Therefore, in the case of periodically deformed plates one can expect accurate numerical results for F from moderate values for the cutoff M, and the convergence is faster for smaller λ.

III. RECTANGULAR CORRUGATION

In the preceding section we developed a nonperturbative approach for computing Casimir interactions between peri-
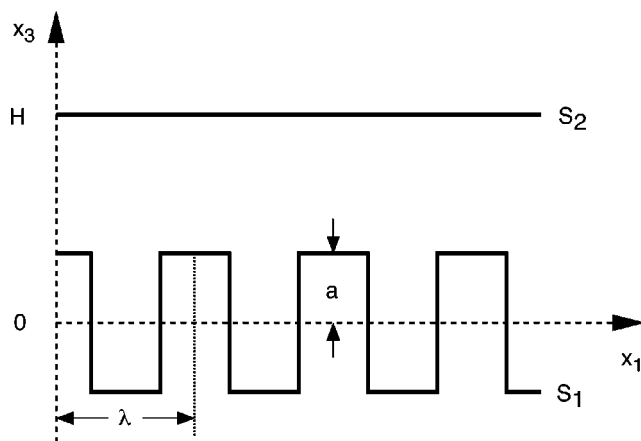
FIG. 2. Geometry consisting of a rectangular corrugated plate and a flat plate. The surfaces are translationally invariant along the x_2 direction.

odically deformed surfaces. In this section we will use the approach to obtain explicit results for the Casimir force between a flat plate and a plate with a rectangular grating. The effect of this class of periodic geometries (corrugated surfaces) can significantly modify the interaction of the objects [35,36]. It was proposed that such geometries can be used to reveal more features of the Casimir interaction [23,24]. For a similar geometry consisting of a sinusoidally corrugated plate and a sphere with a radius $\gg H$, Roy and Mohideen measured the force, and found clear deviations from the predictions of the proximity force approximation [20]. While it has been suggested that lateral shifts of the surfaces caused the discrepancy, we demonstrate below that periodic surfaces allow for a much stronger sensitivity to geometry if the corrugation length is reduced to smaller values. Specifically, we consider the geometry shown in Fig. 2 with a rectangular grating of amplitude a and wavelength λ. Choosing x_1 as the direction of modulation, this corresponds to the height profile

$$h_1(x_1) = \begin{cases} +a & \text{for} \quad |x_1| < \lambda/4 \\ -a & \text{for} \quad \lambda/4 < |x_1| < \lambda/2, \end{cases} \quad (28)$$

and continuation by periodicity $h_1(x_1) = h_1(x_1 + n\lambda)$ for any integer n. The upper plate is flat so that $h_2(x_1) = 0$.

The main purpose of our work is to obtain the Casimir interaction in regimes where other methods such as proximity approximation, pairwise summation of two-body forces, or perturbation theory fail or become unreliable. While the proximity approximation assumes smooth profiles with small local curvature also perturbation theory in the height profile yields divergences in the presence of edges in the profile or if the corrugation length becomes very small, i.e., $\lambda \ll a$, H [25,26]. In perturbation theory, finite corrections of order a^2 are recovered only if edges are "smeared out" over a finite length scale. Thus the correct procedure would be presumably to sum all orders of perturbation theory for a "smeared out" profile, and then to take the limit of sharp edges *after* summing all contributions. Since the perturbative treatment is rather cumbersome the latter program is not practicable, and nonperturbative techniques are imperative.

In order to apply the general result of Eq. (24) for the Casimir force, we have to decompose the matrix $\tilde{\mathcal{M}}$ into the matrices N_m, see Eq. (15). For a general profile, this has to be done by a numerical Fourier transformation. A nice property of the rectangular profile of Eq. (28) is that it allows for an analytical computation of the matrices N_m. The idea is to rewrite the profile of the corrugated plate as a discrete Fourier series,

$$h_1(x_1) = \frac{2a}{\pi} \sum_{n=-\infty}^{\infty} \frac{(-1)^{n-1}}{2n-1} e^{(2\pi i/\lambda)(2n-1)x_1}, \qquad (29)$$

which is inserted into the matrix $\mathcal{M}$ of Eq. (14). Then the Fourier-transformed matrix $\tilde{\mathcal{M}}$ can be calculated, leading after some algebra to the matrices $N_m(q_\perp, q_1)$. Details of this calculation are given in Appendix A. The results are

$$N_{\mathrm{D},m}(q_\perp,q_1) = \begin{cases} \begin{pmatrix} A_m^{\mathrm{D}}(q_\perp,q_1) & 0 \\ 0 & 0 \end{pmatrix} + \delta_{m0} \begin{pmatrix} \dfrac{1}{4q}(1+e^{-2aq}) & \dfrac{e^{-qH}}{2q}\cosh(aq) \\ \dfrac{e^{-qH}}{2q}\cosh(aq) & \dfrac{1}{2q} \end{pmatrix} & \text{for } m \text{ even} \\[3em] \begin{pmatrix} 0 & \dfrac{(-1)^{\frac{m-1}{2}}}{m\pi}\dfrac{e^{-qH}}{q}\sinh(aq) \\ \dfrac{(-1)^{\frac{m-1}{2}}}{m\pi}\dfrac{e^{-\tilde{q}_m H}}{\tilde{q}_m}\sinh(a\tilde{q}_m) & 0 \end{pmatrix} & \text{for } m \text{ odd} \end{cases} \qquad (30)$$

for Dirichlet conditions and

$$N_{\mathrm{N},m}(q_\perp,q_1) = \begin{cases} \begin{pmatrix} A_m^{\mathrm{N}}(q_\perp,q_1) & 0 \\ 0 & 0 \end{pmatrix} + \delta_{m0} \begin{pmatrix} -\dfrac{q}{4}(1+e^{-2aq}) & \dfrac{q}{2}e^{-qH}\cosh(aq) \\ \dfrac{q}{2}e^{-qH}\cosh(aq) & -\dfrac{q}{2} \end{pmatrix} & \text{for } m \text{ even} \\[3em] \begin{pmatrix} 0 & \dfrac{(-1)^{\frac{m-1}{2}}}{m\pi}e^{-qH}\left[q+\dfrac{2\pi m}{\lambda}\dfrac{q_1}{q}\right]\sinh(aq) \\ \dfrac{(-1)^{\frac{m-1}{2}}}{m\pi}e^{-\tilde{q}_m H}\left[\tilde{q}_m-\dfrac{2\pi m}{\lambda}\dfrac{q_1+2\pi m/\lambda}{\tilde{q}_m}\right]\sinh(a\tilde{q}_m) & 0 \end{pmatrix} & \text{for } m \text{ odd} \end{cases}$$

$$(31)$$

for Neumann conditions with

$$A_m^{\mathrm{D}}(q_\perp,q_1) = \frac{1}{\pi^2}\sum_{k=-\infty}^{\infty}\frac{(-1)^{m/2}}{(2k-1)(m-2k+1)}\frac{e^{-2a\tilde{q}_{2k-1}}-1}{\tilde{q}_{2k-1}} \qquad (32)$$

and

$$A_m^{\mathrm{N}}(q_\perp,q_1) = \frac{1}{\pi^2}\sum_{k=-\infty}^{\infty}\frac{(-1)^{m/2}}{(2k-1)(m-2k+1)}\frac{1-e^{-2a\tilde{q}_{2k-1}}}{\tilde{q}_{2k-1}^3}$$

$$\times\left\{q_1\left(q_1+\frac{2\pi m}{\lambda}\right)\left(q_1+\frac{2\pi}{\lambda}(2k-1)\right)^2 \right.$$

$$\left. +2q_\perp^2\left(q_1+\frac{\pi m}{\lambda}\right)\left(q_1+\frac{2\pi}{\lambda}(2k-1)\right)+q_\perp^4\right\}, \qquad (33)$$

respectively, with the definition $\tilde{q}_n = \sqrt{q_\perp^2 + (q_1+2\pi n/\lambda)^2}$, which implies $q \equiv \tilde{q}_0$. With these results at hand, the Casimir force can be calculated by the approach developed in the preceding section. The method is as follows. First, one constructs the matrix B_{kl} of Eq. (17), then one calculates the inverse of B_{kl} to obtain the function $g(q_\perp,q_1)$ of Eq. (22), and finally one has to perform the integration of Eq. (24). In general, this program can only be performed numerically. However, in the limit $\lambda \to 0$ it turns out that a closed form for the function $g(q_\perp,q)$ is available, which allows to obtain the Casimir force in this limit exactly.

A. The limit of small λ

Let us consider the case where the corrugation length λ sets the smallest length scale in the geometry of Fig. 2. If we take the extreme limit of $\lambda \to 0$, a naive assumption is that the field can no longer get into the narrow valleys of the

corrugated plate. Even for small but finite λ this picture should be a good, though approximate, description since it still affects the wavelengths of order H which give the main contribution to the force. Thus one expects that the plates feel a force which is equal to the force between two *flat* plates at the *reduced* distance $H-a$. However, the question remains to what extent this is a good approximation when λ becomes larger, say of order a. To check our naive expectation, we will apply the approach of the preceding section to the limit $\lambda \to 0$. Fortunately, in this limit the matrices $N_m(q_\perp, q_1)$ simplify considerably both for TM and TE modes. The explicit form of these matrices is given in Appendix B. From this result, we can explicitly calculate the functions $g_M(q_\perp, q_1)$ which were introduced before Eq. (25). As explained in Sec. II, the infinite-dimensional matrix B_{kl} is truncated for the calculation at order M with $k, l = -M, \ldots, M$ so that the truncation is done symmetrically around the center at $(k, l) = (0, 0)$ which contains the leading matrix entries. From the exponential convergence behavior of the flat plate result given below [Eq. (27)] one can expect that in the extreme limit $\lambda \to 0$, the series $g_M(q_\perp, q_1)$ converges so rapidly towards $g(q_\perp, q_1)$ that already for $M = 1$ the exact asymptotic expression is obtained. Indeed, our explicit calculation of $g_M(q_\perp, q_1)$ for low M confirms this expectation. From the truncated matrix B_{kl} of Eq. (17) and the matrices of Appendix B we get the simple result

$$g_M(q_\perp, q_1) = \begin{cases} -\dfrac{2q(1+e^{-2aq})}{1+e^{-2aq}-2e^{2(H-a)q}} & \text{for } M = 0 \\ q[\coth(q(H-a))-1] & \text{for } M \geq 1 \end{cases} \tag{34}$$

for both TM and TE modes. Thus from first order ($M = 1$) on the function $g_M(q_\perp, q_1)$ *remains invariant* with increasing dimension M of the matrix B_{kl}. Interestingly, the result for $M \geq 1$ has precisely the form, which one gets for two *flat* plates at reduced distance $H-a$. If one integrates the function $g_M(q_\perp, q_1)$ for $M = 1$ one obtains from Eq. (24) the Casimir force per surface area,

$$F_0/A = -\frac{\pi^2}{480}\frac{1}{(H-a)^4}, \tag{35}$$

for both TM and TE modes. Thus in the limit $\lambda \to 0$ both types of modes yield the same contribution to the total electrodynamic Casimir force $F = 2F_0$. The result of Eq. (35) corresponds to the naive reduced distance argument given at the beginning of this section. Note that this result is nonperturbative in a/H and is exact in the limit $\lambda \to 0$. Perturbation theory for smoothly deformed surfaces always yields corrections to the force of order a^2 [25,26]. However, for small a/H, the result of Eq. (35) has the expansion

$$F_0/A = -\frac{\pi^2}{480}\frac{1}{H^4}\left[1 + 4\frac{a}{H} + O\left(\left(\frac{a}{H}\right)^2\right)\right], \tag{36}$$

which indicates that perturbation theory is not applicable if $\lambda \ll a$. Below we will see that the force F_0 provides an *upper bound* for the Casimir force from both TM and TE modes at fixed H/a, i.e., for increasing λ the force always decreases compared to F_0. We expect that the results of this section for

$\lambda \to 0$ are valid for corrugations of arbitrary shape and also for rough surfaces if λ is identified with the characteristic length scale for surface deformations.

B. The limit of large λ

In the opposite limit of very large λ the corrugated surface is composed of large flat segments with a low density of edges. At sufficiently small surface separations $H \ll \lambda$ the main contribution to the force comes from wavelengths which are much smaller than the scale λ of the surface structure. Thus in the dominant range of mode diffraction can be neglected, and the simple proximity force approximation (Derjaguin approximation [15]) should be applicable. Such an approximation assumes that the total force can be calculated as the sum of local forces between opposite *flat* and *parallel* small surface elements at their local distance $H-h(x_1)$. No distinction is made between TM and TE modes. This procedure is rather simple for the rectangular corrugation considered here since the surface has no curvature (except for edges). There are only two different distances $H+a$, $H-a$ which contribute one-half each across the entire surface area, leading for $\lambda \to \infty$ to the proximity approximation for the force,

$$F_\infty/A = -\frac{\pi^2}{480}\frac{1}{2}\left[\frac{1}{(H-a)^4} + \frac{1}{(H+a)^4}\right]. \tag{37}$$

Below we will see that later result provides a *lower bound* for the Casimir force from both TM and TE modes. In contrast to the limit of small λ the correction for small a/H is of order $(a/H)^2$ here.

C. Numerical analysis

In this section we implement the nonperturbative approach of Sec. II numerically for the rectangular corrugation of Fig. 2. One has to resort to a numerical analysis here since the function $g(q_\perp, q_1)$ cannot be obtained analytically from the matrices of Eqs. (30) and (31) for arbitrary corrugation lengths λ. The numerical procedure follows straightforwardly the computation of the Casimir force in Sec. II. The following implementation applies both to TM and TE modes. At fixed order M, the truncated matrix B_{kl} of Eq. (17) with $k, l = -M, \ldots, M$ is calculated from the matrices N_m of Eqs. (30) and (31). Then the matrix B_{kl} is inverted numerically to yield the function $g_M(q_\perp, q_1)$ from Eq. (22) where the index M denotes the truncation order. Note that the derivative of B_{kl} with respect to H is obtained analytically and no potentially inaccurate numerical derivatives have to be computed. Finally, the integration in Eq. (24) is carried out numerically without difficulty since $g_M(q_\perp, q_1)$ decays exponentially fast for large $q_\perp$, q_1. This provides a series of approximations F_M to the Casimir force which must converge to the exact value of the force as $M \to \infty$. From our analysis of the flat plate geometry, see Eq. (27), we expect an exponentially fast convergence $F - F_M \sim e^{-\gamma M}$ with a coefficient γ. However, the decay coefficient γ depends on the geometrical lengths, and it is expected to increase with decreasing λ/H. This type of convergence behavior was found to be consistent with our

numerical data for F_M. It allowed us to extrapolate the data to obtain the Casimir force F. The largest M for which we calculated F_M was $M=10$ for small $\lambda/a=0.1$ and $M=97$ for large $\lambda/a=300$.

The results of our numerical analysis are as follows. If we express the total Casimir force F or the force contributions F_{TM} and F_{TE} from TM and TE modes, respectively, in units of the corresponding force between two flat plates the results can be expressed in terms of the dimensionless ratios H/a and λ/a only. The results from the extrapolation of the data for F_M are shown in Fig. 3 both for TM and TE modes and different corrugation lengths. For both types of modes the force F_{TM}, F_{TE} is bounded at a fixed plate separation H/a between F_∞ and F_0 as given by Eqs. (37) and (35), respectively. For small λ/a the upper bound F_0 is approached, whereas for asymptotically large λ/a the force converges towards the lower bound F_∞, which is given by the proximity force approximation. Since the convergence towards the lower bound F_∞ becomes slower with increasing H/a there are two distinct scaling regimes for the force at a fixed corrugation length λ/a. At small H/a the relative change of the force compared to the force between two flat plates, $F_T/F_{T,flat}-1$, $T=$TM or TE, decays as $(H/a)^{-2}$. After a crossover regime the relative change of the force decays at larger $H\gg\lambda$ like $(H/a)^{-1}$, following the behavior of the exact result F_0 for $\lambda\to0$. The so far described qualitative behavior of the force is common to both types of modes. However, there is a clear distinction between TM and TE modes, especially at large λ/a, as can be seen from Fig. 3. The force from TE modes has much more pronounced deviation from the proximity approximation result F_∞ as the TM modes. In particular, at large corrugation lengths ($\lambda/a=300$) this can be seen clearly from our numerical data. The same behavior is observed for the deviations from F_0 at small λ/a. Thus, the force F_{TE} appears at intermediate values of λ/a more strongly separated from the lower and upper bounds, cf. Fig. 3(b). We will come back to this point below when we discuss the scaling of the force with λ close to the bounds. Figure 4 shows the total Casimir force in the range of small separations H.

For particular geometries such as a cubic volume the Casimir force has even a different sign for a scalar field with Dirichlet boundary conditions (attractive force) and an electrodynamic field (repulsive force) [16,37]. Since for uniaxial plate deformations both types of fields differ in the presence of a scalar field with Neumann boundary conditions (TE modes) it is interesting to study more quantitatively the difference between the two wave types. Figure 5 shows the ratio F_{TM}/F_{TE} of the forces from both types of modes at different λ/a. One observes that the ratio is peaked at a characteristic H/a which depends on λ/a. For small $H/a\to1$ the ratio tends to 1 as one can expect from the proximity force approximation which does not differentiate between TM and TE modes. In the opposite range of large H/a again both types of modes must contribute almost equally since the geometry approaches that of two flat plates. For the entire range of studied corrugation lengths the ratio converges to one for large H/a according to $|F_{TM}/F_{TE}-1|\sim(H/a)^{-1}$, see Fig. 5(b). However, this asymptotic behavior sets in only beyond a crossover separation H, which increases with λ. At
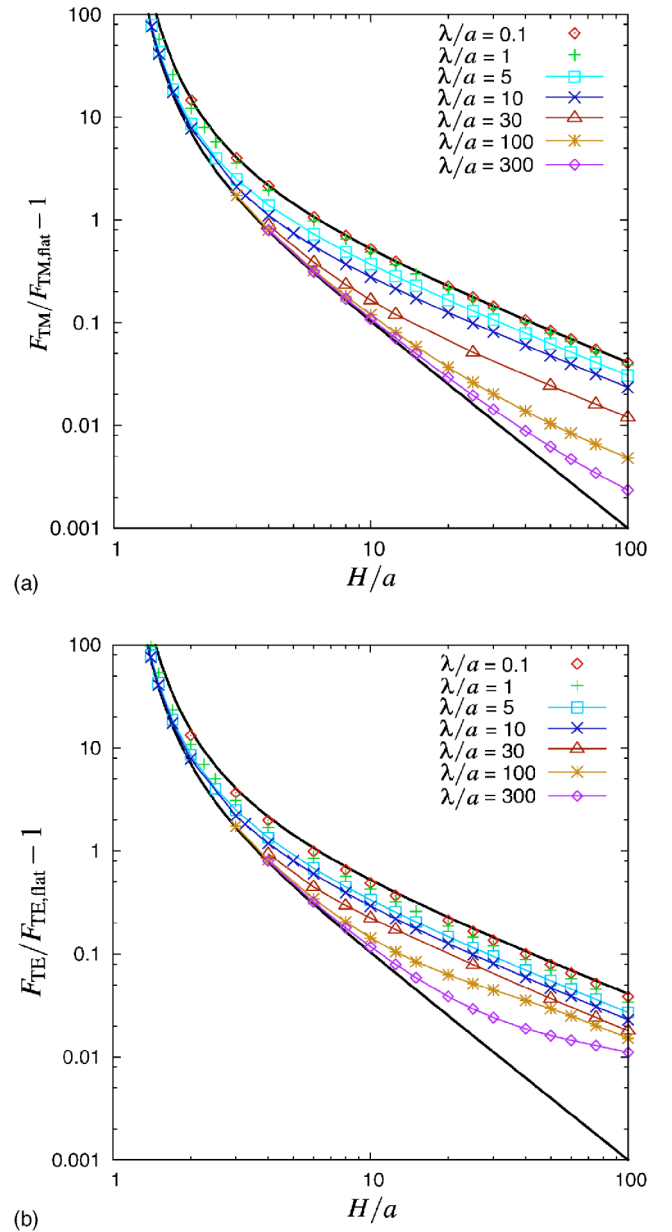
(a)

(b)

FIG. 3. (Color online) Casimir force for TM modes (a) and TE modes (b) as a function of H/a for different corrugation lengths λ/a. Displayed is the change of the force compared to the force between two flat plates, $F_{TM,flat}=F_{TE,flat}=-(\pi^2/480)H^{-4}$, in units of $F_{TM,flat}$ and $F_{TE,flat}$, respectively. The two bold curves enclosing the numerical data are the analytical results F_0 for $\lambda\to0$ (upper curve) and F_∞ for $\lambda\to\infty$ (lower curve), see text.

intermediate λ/a the ratio varies approximately between 0.95 and 1.15 in the studied range of λ/a. TM modes dominate at $\lambda/a\lesssim10$ and at small H/a for all λ/a. The contribution from TE waves is larger for $\lambda/a\gtrsim10$ and $H/a\gtrsim2$. It is instructive to compare this behavior to perturbative results of Refs. [25,26] for the geometry consisting of a *smooth* sinusoidally corrugated and a flat plate. As will be explained in more detail in the following section, the perturbative result for the later geometry yields $F_{TM}/F_{TE}>1$ for all $\lambda/a\gg1$ and $H/a\gg1$, in contrast to our results for the rectangular corrugation. This observation suggests that the corners of the rect-
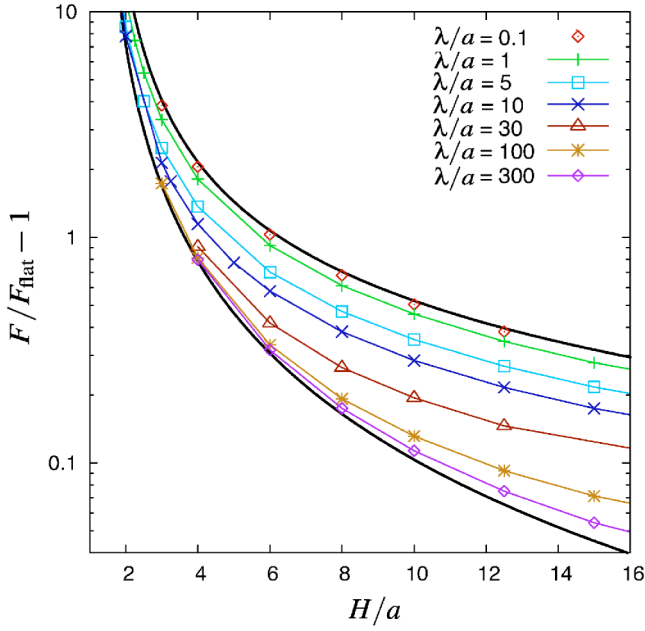
FIG. 4. (Color online) Total Casimir force as sum of TM and TE mode contributions in the short-distance regime. Shown is the relative change of the force compared to the total Casimir force F_{flat} between two flat plates. The data enclosing bold curves have the same meaning as in Fig. 3, but for the total force they are now given by $2F_0$ and $2F_\infty$ due to the same contribution of TM and TE modes in these two limits.

angular corrugation in fact cause the slight amplification of TE modes compared to TM waves at $\lambda/a \gtrsim 10$. One can argue that imposing for TE modes a vanishing normal derivative on the field at the concave corners inside the valleys of the corrugation provides a stronger constraint on field fluctuations as compared to Dirichlet conditions for TM modes. If the width of the valleys is decreased with λ, the two opposite corners can no longer be considered separately and the Dirichlet condition might provide a stronger restriction. For very small H/a the main contribution to the force comes from rather short wavelengths which should be only very weakly affected by the Neumann conditions at the concave corners.

Finally, we consider the scaling of the force from TM and TE modes close to lower and upper bounds F_∞ and F_0, respectively. Figures 6 and 7 show a logarithmic plot of force form TM and TE modes at fixed $H=10a$ and $H=100a$, measured relative to F_∞ for large λ/a and relative to F_0 for small λ/a. At small λ we found an interesting qualitative difference between TM and TE modes for the scaling towards the exact result F_0 for $\lambda \to 0$,

$$\frac{F_0 - F_{\text{TM}}}{F_{\text{TM,flat}}} \sim \frac{\lambda}{a}, \quad \frac{F_0 - F_{\text{TE}}}{F_{\text{TE,flat}}} \sim \left(\frac{\lambda}{a}\right)^{1/2}. \quad (38)$$

For the change in the exponents we cannot present a satisfying simple argument. In the opposite limit of large λ the proximity approximation result F_∞ is approached linearly for both types of modes,
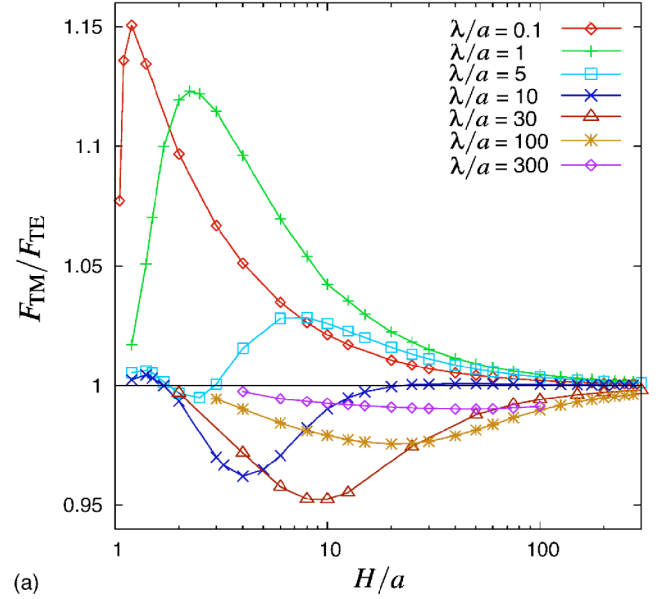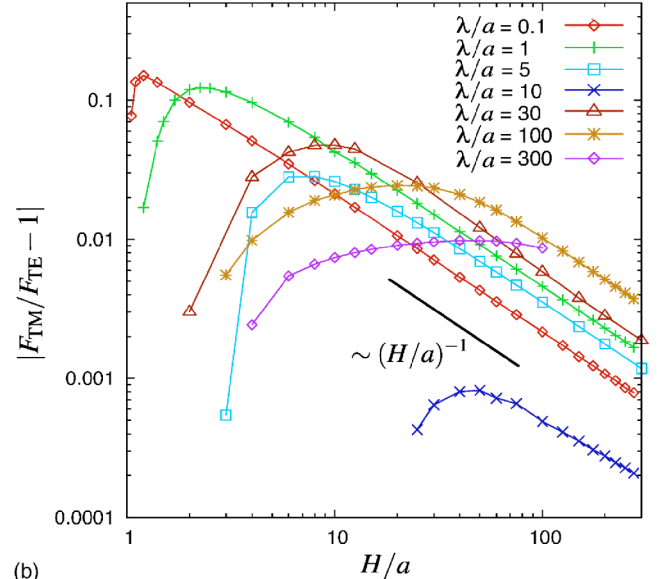

FIG. 5. (Color online) (a) Ratio of Casimir force from TM and TE modes as a function of the plate distance H for different corrugation lengths λ. (b) Logarithmic plot of the deviation of the ratio from one at large H.

$$\frac{F_{\text{TM}} - F_\infty}{F_{\text{TM,flat}}} \sim \frac{a}{\lambda}, \quad \frac{F_{\text{TE}} - F_\infty}{F_{\text{TE,flat}}} \sim \frac{a}{\lambda}. \quad (39)$$

As we will show in the following section, this linear decrease can be understood in terms of geometric optics.

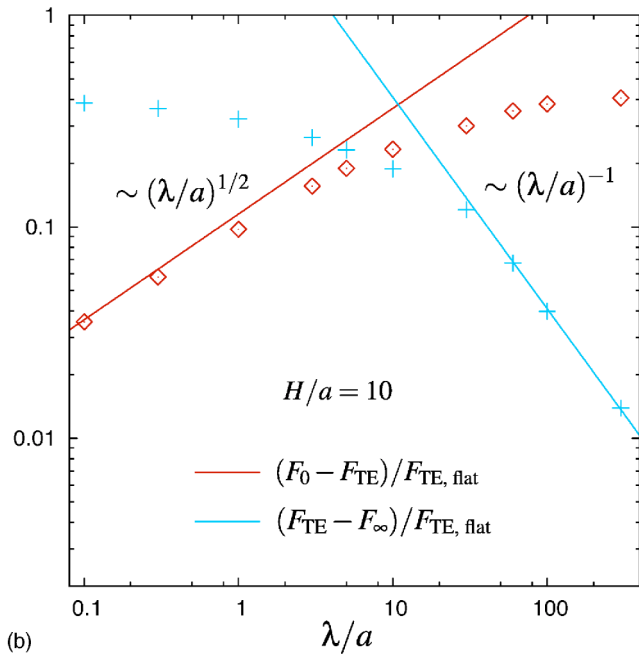## IV. COMPARISON WITH PERTURBATION THEORY AND GEOMETRIC OPTICS

The aim of this section is to compare the numerical results of the preceding section to those which were obtained from perturbation theory in Refs. [25,26] for a uniaxially and sinusoidally corrugated surface. We will show that discrepancies in the results from the two approaches can be qualita-
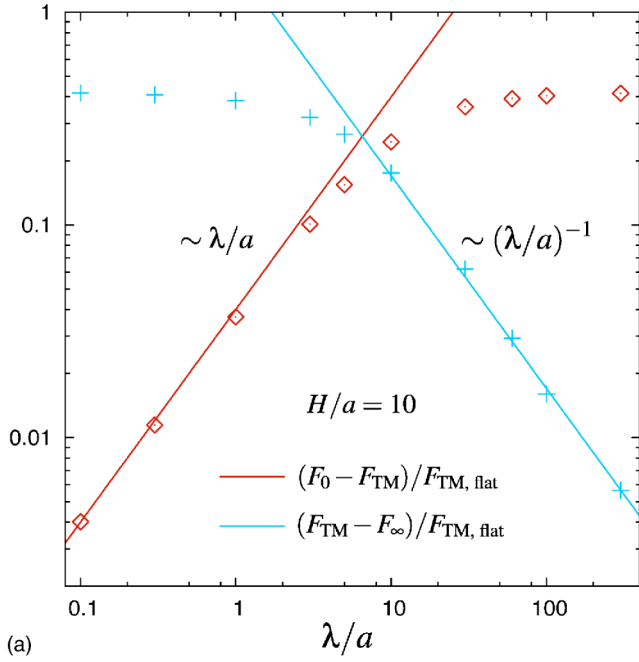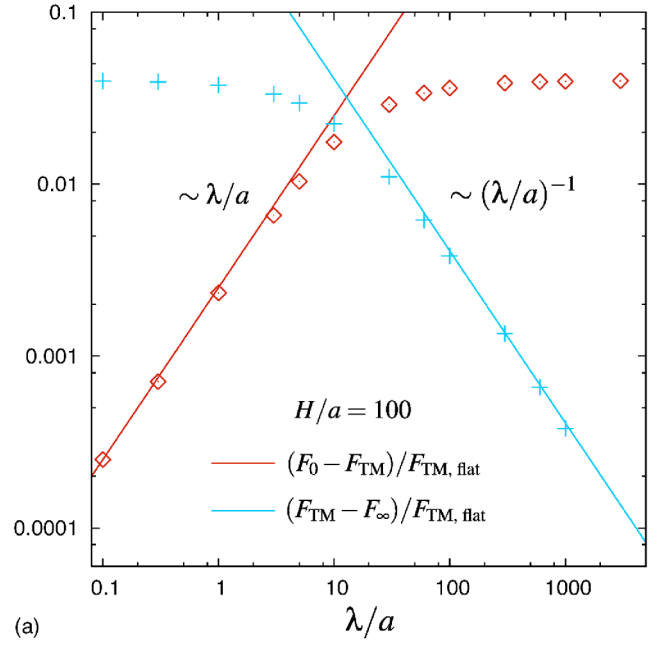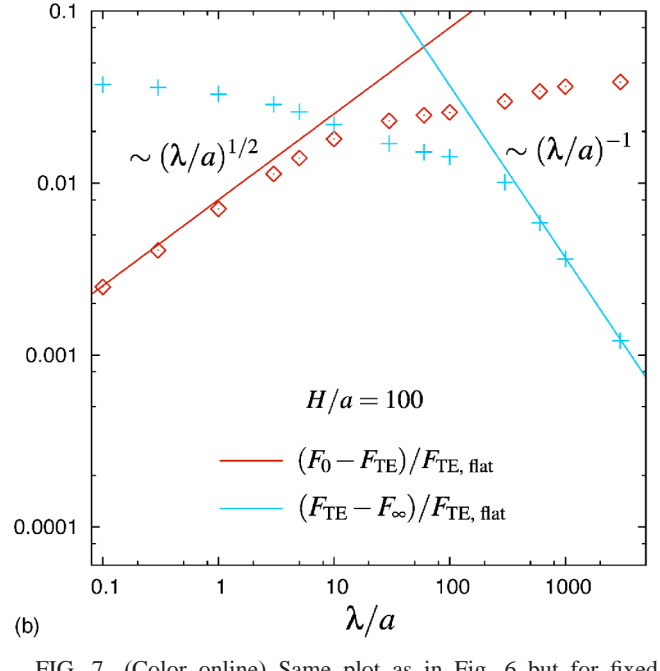
FIG. 6. (Color online) Scaling of the force from TM (a) and TE (b) modes close to the upper bound F_0 ($\lambda \to 0$) and the lower bound F_∞ ($\lambda \to \infty$) as a function of λ/a at fixed mean surface distance $H = 10a$. Forces are measured in units of $F_{\text{TM,flat}}$ and $F_{\text{TE,flat}}$, respectively.

tively understood in terms of classical ray optics, a concept which was introduced in Ref. [28] for the computation of Casimir interactions. In the perturbational path-integral approach, the logarithm of the partition function is expanded in powers of the height profile h_1 as $\ln \mathcal{Z} = \ln \mathcal{Z}|_0 + \ln \mathcal{Z}|_1 + \ln \mathcal{Z}|_2 + \cdots$. The zero-order term $\ln \mathcal{Z}|_0 = (\pi^2/720) ALH^{-3}$ is the result for flat planes. The first-order correction vanishes, $\ln \mathcal{Z}|_1 = 0$, since h_1 is on spatial average zero, and the second-order contribution reads

FIG. 7. (Color online) Same plot as in Fig. 6 but for fixed distance $H = 100a$.

$$\ln \mathcal{Z}_2 = \frac{\pi^2 L}{240 H^5} \int_{\mathbf{x}_\parallel} h_1^2(x_1) - \frac{L}{4} \int_{\mathbf{x}_\parallel} \int_{\mathbf{x}_\parallel'} K(|\mathbf{x}_\parallel - \mathbf{x}_\parallel'|)$$
$$\times [h_1(x_1) - h_1(x_1')]^2. \tag{40}$$

where $K(|\mathbf{x}_\parallel - \mathbf{x}_\parallel'|)$ denotes a response kernel which has contributions from both TM and TE modes and was obtained in Ref. [26]. The second term is only finite for a smooth profile $h_1(x_1)$ since the kernel has a singularity $\sim |\mathbf{x}_\parallel - \mathbf{x}_\parallel'|^{-3}$. Thus for a rectangular corrugation with $\int_{\mathbf{x}_\parallel} [h_1(x_1) - h_1(x_1 + x_1')]^2 \sim |x_1'|$ for $|x_1'| < \lambda/4$ the perturbative result diverges due to the presence of sharp edges in the surface profile. In contrast, for a
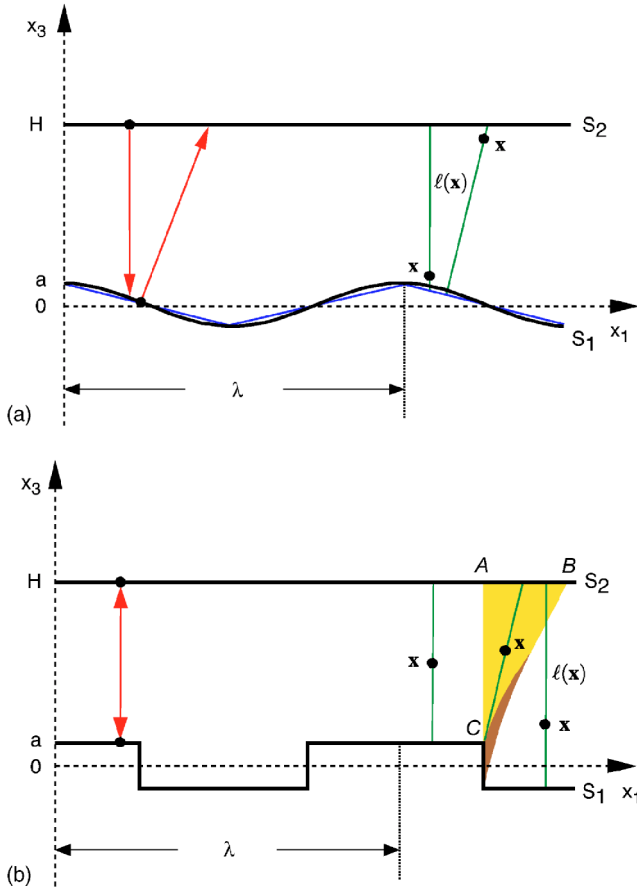
FIG. 8. (Color online) Typical paths of the proximity force approximation and the geometric optics approach for both sinusoidal (a) and rectangular corrugation (b) with $\lambda \gg a$. Paths with arrows denote distances which are measured normal to one of the surfaces as used for the proximity force approximation. Paths without arrows denote the shortest surface connecting paths of length $\ell(\mathbf{x})$ through a point $\mathbf{x}$ located in the gap between the plates.

sinusoidal profile with $h_1(x_1) = a \cos(2\pi x_1/\lambda)$ one has $\int_{\mathbf{x}_\parallel} [h_1(x_1) - h_1(x_1+x_1')]^2 \sim x_1'^2$ and the divergence of the kernel is compensated. For this reason, we compare our numerical results for the rectangular corrugation to the perturbative results for a sinusoidal profile [25,26]. This will allow us to study the influence of edges on the Casimir interaction. Perturbation theory yields for the total Casimir force of the sinusoidal geometry of Fig. 8(a) the result

$$F = F_{\text{flat}} \left[1 + \tilde{G}\left(\frac{H}{\lambda}\right)\left(\frac{a}{H}\right)^2 + O(a^3) \right], \qquad (41)$$

with the function parameter free $\tilde{G}(u) = (480/\pi^2)[5G(u) - uG'(u)]$, where $G(u) = G_{\text{TM}}(u) + G_{\text{TE}}(u)$ has contributions from TM and TE modes; for the explicit form of $G(u)$ see Ref. [26]. For comparison with our numerical results the limits of small and large H/λ are of particular interest. From an expansion of $\tilde{G}(u)$ one obtains the asymptotic expressions

$$\frac{F}{F_{\text{flat}}} - 1 = \begin{cases} \dfrac{8\pi}{3}\dfrac{a}{\lambda}\dfrac{a}{H} & \text{for } \lambda \ll H \\[2ex] 5\left(\dfrac{a}{H}\right)^2 + \left(\dfrac{4\pi^2}{3} - 20\right)\left(\dfrac{a}{\lambda}\right)^2 & \text{for } \lambda \gg H. \end{cases}$$

$$(42)$$

In both limits the results are valid only if $a \ll \lambda$. In the limit of small λ/a there is a divergence $\sim a/\lambda$ in the perturbative result, which reflects the above-mentioned divergence in Eq. (40) for rectangular corrugations with vertical segments. This singularity does not appear in our numerical results of the preceding section; it is a characteristic feature of perturbation theory. In the following comparison we consider only the case $\lambda \gg a$. Equation (42) suggests for large plate separations $H \gg \lambda$ a decay of the excess force from the corrugation $\sim a/H$ and for small H/λ a decay $\sim (a/H)^2$. The scaling behavior is in agreement with our observations for the rectangular corrugation as demonstrated in Fig. 3. However, the latter figure also shows that for smaller $\lambda/a \lesssim 10$ the scaling regime with a decay $\sim (a/H)^2$ does not exist.

Next, we will compare the perturbative results of Eq. (42) with our numerical results for the deviation of the actual Casimir force from the proximity force approximation (PA), $(F-F_{\text{PA}})/F_{\text{flat}}$, where F_{PA} is the force obtained from the PA. This approximation does no distinguish between the two types of modes and thus for the rectangular corrugation one has $F_{\text{PA}} = 2F_\infty$, with F_∞ given by Eq. (37). In general, for deformed surfaces the PA is ambiguous [28] since the pairs of small parallel surface elements can be chosen to be parallel to either surface so that the local plate distance is measured either normal to S_1 or normal to S_2 as indicated by the arrows of Fig. 8. We emphasize that this ambiguity does not arise for the rectangular corrugation. For smooth surfaces with finite curvature such as a sinusoidal corrugation the PA result depends on the reference plate. If one measures the local distance perpendicular to the flat surface, as it is most common, one obtains for the Casimir energy per surface area,

$$\mathcal{E}_{\text{PA}} = \frac{1}{A} \int_{S_2} dS \, \mathcal{E}_{\text{flat}}(H - h_1(x_1)), \qquad (43)$$

but if the local distances are chosen perpendicular to the corrugated plate, one has

$$\mathcal{E}_{\text{PA,corr}} = \frac{1}{A} \int_{S_1} dS \, \mathcal{E}_{\text{flat}}((H - h_1(x_1))\sqrt{1 + [h_1'(x_1)]^2}), \qquad (44)$$

where $\mathcal{E}_{\text{flat}}(H) = -(\pi^2/720)H^{-3}$ is the Casimir energy per surface area for two flat surfaces. For a sinusoidal corrugation the integrals over the surfaces can be computed perturbatively in a. This yields for large λ the difference between the force F from perturbation theory [Eq. (42)] and the PA force, based on the flat and the corrugated plate, respectively,

$$\frac{F - F_{\mathrm{PA}}}{F_{\mathrm{flat}}} = \left(\frac{4\pi^2}{3} - 20\right)\left(\frac{a}{\lambda}\right)^2,$$

$$\frac{F - F_{\mathrm{PA,corr}}}{F_{\mathrm{flat}}} = \left(\frac{10\pi^2}{3} - 20\right)\left(\frac{a}{\lambda}\right)^2. \tag{45}$$

The essential result is that the perturbatively obtained force approaches the PA approximation like $(a/\lambda)^2$ for large λ which has to be compared to the a/λ decay seen in our numerical results for the rectangular corrugation, cf. Figs. 6 and 7. Thus the deviation from the PA is stronger for the rectangular corrugation than for the sinusoidal profile, presumably due to sharp edges. Before we give a simple physical argument for the variation of the decay exponent, let us compare the amplitudes in Eq. (45). If we chose the PA to be based on the flat plate, the amplitude is negative, and the force F_{PA} is *not* a lower bound to the force at a fixed H/a, in disagreement with our observation for a rectangular corrugation. The corrugated surface based PA in contrast yields a positive amplitude. We expect that also for a sinusoidal corrugation the actual force is monotonous in λ/a at fixed H/a, assuming its minimal value for $\lambda/a \to \infty$. The change of sign is just another manifestation of the ambiguity in the proximity approximation. The observation that the actual Casimir force is located between the flat and the curved surface based PA was also made for a plane plate-sphere geometry recently [38].

In order to understand the dependence of the exponent for the scaling towards the PA limit on the shape of the corrugation, it is instructive to consider classical ray optics. Such an approach was recently applied to the calculation of Casimir interactions [28]. Since this approach does not take diffraction into account it is limited to deformations where the radii of curvature are large compared to the smallest distance between the surfaces. But still, geometric optics allow for a better description of Casimir forces than the conventional proximity force approximation. By considering instead of all actual optical paths only the *shortest* paths, Jaffe and Scardicchio proposed an "optimal" proximity approximation for scalar field fluctuations subject to Dirichlet boundary conditions [28]. It can be also applied to electromagnetic fields. Consider a position $\mathbf{x}$ in the vacuum space between the plates, and denote by $\ell(\mathbf{x})$ the length of the shortest optical ray between the plates through that point. Figure 8 shows typical paths for the two types of corrugations we consider here. The Casimir energy in this optical approximation can then be written as

$$\frac{\mathcal{E}_{\mathrm{opt}}}{\mathcal{E}_{\mathrm{flat}}} = \int d^2\mathbf{x}_{\parallel} \int_{h_1(x_1)}^{H} dx_3 \frac{H^3}{A\ell^4(\mathbf{x}_{\parallel},x_3)}, \tag{46}$$

where the integral runs over the total space between the surfaces.

First, we apply this approach to the sinusoidal profile, see Fig. 8(a). For simplicity, we replace the sinusoidal profile by a piecewise linear profile, cf. Fig. 8(a), which is a good approximation in the limit $a \ll \lambda$ considered here. Then we have to determine $\ell(\mathbf{x})$ for each position between the plates for this simpler profile. Since the exact value for $\ell(\mathbf{x})$ is difficult

to evaluate, we consider the two cases where the position is close to one of the two surfaces and then assume a linear interpolation between the two lengths for $\ell(\mathbf{x})$ at arbitrary $\mathbf{x}$ in the gap between the plates. If $\mathbf{x}$ is very close to the deformed surface S_1 the shortest path is perpendicular to the flat surface S_2. On the contrary, if $\mathbf{x}$ is located close to the flat surface S_2, the shortest ray is perpendicular to the deformed surface S_1. With the so obtained approximative lengths $\ell(\mathbf{x})$ we obtain from Eq. (46) by expansion in a/H for the correction to the flat surface based proximity approximation the scaling behavior

$$\frac{F_{\mathrm{opt}} - F_{\infty}}{F_{\mathrm{flat}}} \sim \left(\frac{a}{\lambda}\right)^2. \tag{47}$$

Thus the optical approach nicely reproduces the correct scaling of the corrections to the proximity approximation at large λ, in agreement with the perturbative result of Eq. (45).

In order to examine the role of edges for deviations from the proximity approximation, we apply the optical approach also to the rectangular corrugation in Fig. 8(b). For this geometry the shortest paths are easily identified. Except for positions located in an almost triangular shaped region [composed of the two shaded regions of Fig. 8(b)] the paths are just perpendicular to both surfaces. Thus the deviation from the proximity approximation is caused by paths through points which are located inside the shaded region. These paths run either to corner C of the surface (larger region) or to the vertical surface segment (smaller region). For sufficiently large λ the regions from adjacent edges do not overlap and can be treated independently. Furthermore, since the ratio of the area of the larger shaded region formed by the triangle ABC and the area of the smaller shaded region bounded by the vertical surface segment scales like $\sim(H/a)^2$, one has to consider only the triangle ABC for the evaluation of Eq. (46) in the limit $a/H \ll 1$. This gives

$$\frac{F_{\mathrm{opt}} - F_{\infty}}{F_{\mathrm{flat}}} \sim \sqrt{\frac{a}{H}}\frac{a}{\lambda}. \tag{48}$$

This result is in agreement with the scaling behavior we have observed in our nonperturbative approach for the rectangular profile; see Figs. 6 and 7, and Eq. (39). We conclude that the analysis of the *shortest* optical paths explains the observed dependence of the Casimir force on the surface shape close the proximity force limit $\lambda \gg H$.

Finally, we consider the ratio $F_{\mathrm{TM}}/F_{\mathrm{TE}}$ of the force contributions from TM and TE modes. In perturbation theory one obtains from the separate contributions of the two types of modes to the result of Eq. (41) the low a expansion

$$\frac{F_{\mathrm{TM}}}{F_{\mathrm{TE}}} = 1 + \frac{8\pi}{3}\frac{a}{\lambda}\frac{a}{H}, \tag{49}$$

which is valid if both $H \gg \lambda$ and $\lambda \gg a$. Thus for sinusoidal corrugations the force has always larger contributions from TM modes at asymptotically large H, in contrast to our numerical results for rectangular corrugations, cf. Fig. 5(a). We argued in the preceding section that edges might cause the amplification of TE mode contributions. However, the con-

vergence of the ratio to one for large H turns out be insensitive to the shape of the corrugations. Our numerical results agree perfectly over the full range of studied λ/a with perturbation theory in that the ratio decays like a/H to one, see Fig. 5(b). For small $\lambda/a \to 0$ the amplitude in no longer given by Eq. (49) but saturates at a finite value which decreases with λ since for $\lambda \to 0$ the reduced distance argument of Sec. III A implies equal contributions from both types of modes.

V. CONCLUSIONS AND FURTHER APPLICATIONS

In this paper we have developed a nonperturbative method to compute Casimir interactions in periodic geometries. This approach is based on a path-integral quantization of the electromagnetic field subject to ideal metal boundary conditions. The so obtained effective action for the Casimir interaction is transformed to a representation which is adapted to periodic geometries and allows for an efficient numerical computation of the force between macroscopic objects. In particular, the approach allows us to compute the Casimir force between surfaces with *strong* periodic deformations and edges. For uniaxial deformations the electromagnetic field can be decomposed into two scalar fields which are subject to Dirichlet and Neumann boundary conditions, respectively. This enables us to study qualitative differences in the geometry dependence of the Casimir interaction for scalar fields with different boundary conditions. Applications of the latter case range from thermal fluctuations in superfluids to liquid crystals [30,31] which can be described by a scalar field. Path-integral quantization in the presence of boundaries has been previously applied to perturbative calculations of Casimir interactions between static and dynamic deformed manifolds in the context of both thermal [30,31] and quantum fluctuations [23–26] of the confined field. However, all these computations were restricted to slightly deformed surfaces and edges were excluded. While a number of qualitative predictions of perturbation theory are confirmed by our approach even for strong deformations, we find nonperturbative effects which were unaccessible previously.

As an explicit example, we calculated by the Casimir interaction between a flat and a rectangular corrugated plate with edges, including the case of large deformation amplitudes. Arbitrary periodic profiles can be treated by our approach as well by Fourier transforming the kernel of the effective action numerically and then applying the same technique we used here for the rectangular corrugation. We could confirm the perturbatively predicted existence of two different scaling regimes for the deformation-induced part of the interaction as a function of the mean plate separation H. However, we also find that for small corrugation lengths only the large H scaling regime exists. We demonstrate by explicit calculations that in the limit of very small corrugation lengths the force can be obtained as the interaction of two flat surfaces with a reduced distance. At very large corrugation length and small H we find that the force approaches the result of the proximity force approximation. Our approach also allowed for a precise computation of the scaling of the
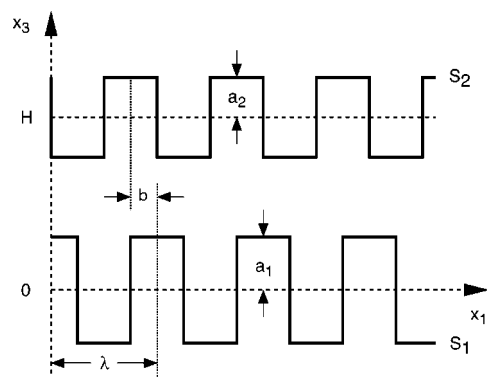

FIG. 9. Two rectangular corrugated plates with the same wavelength λ but different amplitudes a_1 and a_2 and a lateral shift of b. The plates are translationally invariant along the x_2 direction.

force close to the limits of small and large corrugation length which provide an upper and lower bound, respectively, to the force. In both cases we find power-law scaling with λ/a, rendering corrections to proximity approximation in general large. The exponents of these power laws depend on the type of modes (transversal electric or magnetic) for small corrugation length. At large corrugation length we find an interesting dependence of the exponents on generic features of the corrugations. By comparison with perturbation theory for a sinusoidal corrugation we find that edges induce a slower decay towards the prediction of the proximity approximation as compared to smooth profiles. We could explain this generic behavior in terms of classical optical paths.

Our nonperturbative method can be applied to a number of other interesting situations. Since the path-integral technique can be used in arbitrary dimensions of the embedding space and the surfaces, our method can be also used in this general case. In this paper we focused on uniaxial deformations. Two directional corrugations can also be treated by our method by applying it to the full electromagnetic gauge field without splitting into TM and TE modes. The latter case could help to understand the possibility of repulsive forces since plates with two directional corrugations form at short-distance cavities, i.e., geometrical shapes similar to a sphere for which a repulsive "force" is expected [16]. At short plate separations, material properties become in general important for the interaction. These effects can be also described by a path-integral approach with nonlocal boundary conditions [39], enabling the application of the methods developed here. For two corrugated surfaces, the existence of a lateral Casimir force has been predicted and computed by perturbative techniques [23,26]. It would be interesting to study the effect of *strong* corrugations and edges on the lateral Casimir effect by our method. For the dynamic Casimir effect the surfaces are *dynamically* deformed, which leads for oscillations in time again to corrugated surfaces in Euclidean space, but now along imaginary time. Our results thus imply different behavior at small and large frequencies.

APPENDIX A: FOURIER TRANSFORM OF THE RECTANGULAR CORRUGATION MODEL

We calculate the Fourier-transformed matrices $\widetilde{\mathcal{M}}$ for Dirichlet and Neumann boundary conditions for a slightly more general geometry with two corrugated plates. Both plates are assumed to have a rectangular corrugation profile with the same wavelength λ, but with different amplitudes a_1 and a_2. This geometry is depicted in Fig. 9, and the geometry of the system discussed in Sec. III is obtained by simply setting the amplitude of the second plate to zero. The reason to perform this calculation here is that it is more transparent than the calculation which assumes one corrugated and one flat plate. In addition, we allow the plates to have a lateral displacement b.

We start with the matrix for Dirichlet boundary conditions, cf. Eq. (14a). Performing first the Fourier transformation with respect to $\mathbf{x}_\perp = (x_0, x_2)$, we have

$$\widetilde{\mathcal{M}}_D^{\alpha\beta}(\mathbf{p},\mathbf{q}) = \int_{\mathbf{x}_\perp} \int_{\mathbf{y}_\perp} \int_{x_1} \int_{y_1} e^{i\mathbf{p}_\perp \cdot \mathbf{x}_\perp + i\mathbf{q}_\perp \cdot \mathbf{y}_\perp} e^{ip_1 x_1 + iq_1 y_1} \mathcal{G}[\mathbf{x}_\perp - \mathbf{y}_\perp, x_1 - y_1; h_\alpha(x_1) - h_\beta(y_1) + H(\delta_{\alpha 2} - \delta_{\beta 2})]$$

$$= (2\pi)^2 \delta^{(2)}(\mathbf{p}_\perp + \mathbf{q}_\perp) \int_{x_1} \int_{y_1} \int_{p_1'} e^{i(p_1 - p_1')x_1 + i(q_1 + p_1')y_1} \frac{e^{-\sqrt{p_\perp^2 + p_1'^2}|h_\alpha(x_1) - h_\beta(y_1) + H(\delta_{\alpha 2} - \delta_{\beta 2})|}}{2\sqrt{p_\perp^2 + p_1'^2}} \tag{A1}$$

To evaluate this last expression analytically, it is necessary to find a simplified expression for the dependence of the second exponential term on x_1 and y_1. At this point, the use of piecewise constant profiles for the material plates becomes crucial. Since $h_\alpha = \pm a_\alpha$, for $\alpha = \beta$ we can write

$$e^{-\tilde{p}|h_\alpha(x_1) - h_\alpha(y_1)|} = e^{-a_\alpha \tilde{p}}[\cosh(a_\alpha \tilde{p}) + a_\alpha^{-2} h_\alpha(x_1) h_\alpha(y_1)\sinh(a_\alpha \tilde{p})]. \tag{A2}$$

Similarly, for $\alpha \neq \beta$, we get

$$e^{-\tilde{p}|h_\alpha(x_1) - h_\beta(y_1) + H(\delta_{\alpha 2} - \delta_{\beta 2})|} = e^{-\tilde{p}H}[\cosh(a_\alpha \tilde{p}) - (-1)^\alpha a_\alpha^{-1} h_\alpha(x_1)\sinh(a_\alpha \tilde{p})][\cosh(a_\beta \tilde{p}) - (-1)^\beta a_\beta^{-1} h_\beta(y_1)\sinh(a_\beta \tilde{p})]. \tag{A3}$$

To keep the notation short, we introduced $\tilde{p} = \sqrt{p_\perp^2 + p_1'^2}$. Now, we insert the Fourier series expression for h_α, given by

$$h_\alpha(x_1) = \frac{2a_\alpha}{\pi} \sum_{n=-\infty}^{\infty} \frac{(-1)^{n-1}}{2n-1} e^{(2\pi i/\lambda)(2n-1)(x_1 + \delta_{\alpha 2} b)} \tag{A4}$$

into the right-hand side (rhs) of Eqs. (A2) and (A3). Then, inserting those into Eq. (A1), the remaining integrals over x_1, y_1, and p_1' can easily be performed. This yields the periodic formula

$$\widetilde{\mathcal{M}}_D(\mathbf{p},\mathbf{q}) = (2\pi)^3 \delta^{(2)}(\mathbf{p}_\perp + \mathbf{q}_\perp) \sum_{m=-\infty}^{\infty} \delta(p_1 + q_1 + 2\pi m/\lambda) N_{D,m}(q_\perp, q_1), \tag{A5}$$

with the matrices

$$N_{D,m}(q_\perp, q_1) = \begin{pmatrix} A_{m,1}^D(q_\perp, q_1) & B_{m,12}^D(q_\perp, q_1) \\ \gamma^m B_{m,21}^D(q_\perp, q_1) & \gamma^m A_{m,2}^D(q_\perp, q_1) \end{pmatrix} + \delta_{m0} \begin{pmatrix} \dfrac{1}{4q}(1 + e^{-2a_1 q}) & \dfrac{e^{-qH}}{2q}\cosh(a_1 q)\cosh(a_2 q) \\ \dfrac{e^{-qH}}{2q}\cosh(a_1 q)\cosh(a_2 q) & \dfrac{1}{4q}(1 + e^{-2a_2 q}) \end{pmatrix} \tag{A6}$$

for m even, and

$$N_{D,m}(q_\perp, q_1) = \begin{pmatrix} 0 & C_{m,12}^D(q_\perp, q_1) \\ C_{m,21}^D(q_\perp, q_1) & 0 \end{pmatrix} \tag{A7}$$

for m odd. The entries of the matrices are given as follows:

$$A_{m,\alpha}^D(q_\perp, q_1) = \frac{(-1)^{m/2}}{\pi^2} \sum_{k=-\infty}^{\infty} \frac{1}{(m - 2k + 1)(2k - 1)} \frac{e^{-2a_\alpha \tilde{q}_{2k-1}} - 1}{\tilde{q}_{2k-1}}, \tag{A8}$$

$$B_{m,\alpha\beta}^D(q_\perp, q_1) = 2\frac{(-1)^{m/2}}{\pi^2} \sum_{k=-\infty}^{\infty} \frac{\gamma^{(2k-1)(\delta_{\beta 2} - \delta_{\alpha 2})}}{(m - 2k + 1)(2k - 1)} \frac{e^{-\tilde{q}_{2k-1} H}}{\tilde{q}_{2k-1}} \sinh(a_\alpha \tilde{q}_{2k-1})\sinh(a_\beta \tilde{q}_{2k-1}), \tag{A9}$$

and

$$
C^{\mathrm{D}}_{m,\alpha\beta}(q_{\perp},q_1) = \frac{(-1)^{(m+1)/2}}{m\pi}\left[(-1)^{\alpha}\gamma^{m\delta_{\alpha2}}\frac{e^{-qH}}{q}\sinh(a_{\alpha}q)\cosh(a_{\beta}q) + (-1)^{\beta}\gamma^{m\delta_{\beta2}}\frac{e^{-\tilde{q}_mH}}{\tilde{q}_m}\sinh(a_{\beta}\tilde{q}_m)\cosh(a_{\alpha}\tilde{q}_m)\right], \quad (A10)
$$

where the phase factor $\gamma=e^{2\pi ib/\lambda}$ was introduced. We note that the off-diagonal entries $B^{\mathrm{D}}_{m,\alpha\beta}$ and $C^{\mathrm{D}}_{m,\alpha\beta}$ implicitly depend on b through γ. Furthermore, $\tilde{q}_n=\sqrt{q_1^2+(q_1+2\pi n/\lambda)^2}$ was introduced, which implies $q\equiv\tilde{q}_0$. If $a_2=0$, the matrices $N_{\mathrm{D},m}$ have the symmetry $N_{\mathrm{D},m}(q_{\perp},-q_1)=N_{\mathrm{D},-m}(q_{\perp},q_1)$, and analogously for the Neumann matrices $N_{\mathrm{N},m}$, which we used in Sec. II. We remark that this symmetry is no longer valid for either type of boundary conditions if $h_2(x_1)\neq h_2(-x_1)$.

The matrix $\widetilde{\mathcal{M}}_{\mathrm{N}}$ for the Neumann boundary condition is obtained similarly, as for the Dirichlet boundary condition. Evaluating first the Fourier transform of the orthogonal components as done in expression (A1), the result is

$$
\widetilde{M}^{\alpha\beta}_{\mathrm{N}}(\mathbf{p},\mathbf{q}) = (2\pi)^2\delta^{(2)}(\mathbf{p}_{\perp}+\mathbf{q}_{\perp})\int_{x_1}\int_{y_1}e^{ip_1x_1+iq_1y_1}(-1)^{\alpha+\beta}\{-\partial^2_{x_3}+[h'_{\alpha}(x_1)+h'_{\beta}(y_1)]\partial_{x_1}\partial_{x_3}-h'_{\alpha}(x_1)h'_{\beta}(y_1)\partial^2_{x_1}\}
$$

$$
\times\int_{p'_1}e^{-ip'_1(x_1-y_1)}\left.\frac{e^{-\sqrt{p_{\perp}^2+p_1'^2}|x_3-y_3|}}{2\sqrt{p_{\perp}^2+p_1'^2}}\right|_{\substack{x_3=h_{\alpha}(x_1)+H\delta_{\alpha2}\\ y_3=h_{\beta}(y_1)+H\delta_{\beta2}}}
$$

$$
= (2\pi)^2\delta^{(2)}(\mathbf{p}_{\perp}+\mathbf{q}_{\perp})\int_{x_1}\int_{y_1}\int_{p'_1}e^{i(p-p'_1)x_1+i(q_1+p'_1)y_1}\frac{(-1)^{\alpha+\beta}}{2}\left[-\sqrt{p_{\perp}^2+p_1'^2}-\frac{ip'_1}{\sqrt{p_{\perp}^2+p_1'^2}}(\partial_{x_1}-\partial_{y_1})\right.
$$

$$
\left.-\frac{p_1'^2}{(p_{\perp}^2+p_1'^2)^{3/2}}\partial_{x_1}\partial_{y_1}\right]\times e^{-\sqrt{p_{\perp}^2+p_1'^2}|h_{\alpha}(x_1)-h_{\beta}(y_1)+H(\delta_{\alpha2}-\delta_{\beta2})|}. \tag{A11}
$$

We apply partial integration to obtain

$$
\widetilde{\mathcal{M}}^{\alpha\beta}_{\mathrm{N}}(\mathbf{p},\mathbf{q}) = (2\pi)^2\delta^{(2)}(\mathbf{p}_{\perp}+\mathbf{q}_{\perp})\frac{(-1)^{\alpha+\beta}}{2}\int_{p'_1}\left[-\sqrt{p_{\perp}^2+p_1'^2}-\frac{p'_1}{\sqrt{p_{\perp}^2+p_1'^2}}(p_1-q_1-2p'_1)+\frac{p_1'^2}{(p_{\perp}^2+p_1'^2)^{3/2}}(p_1-p'_1)(q_1+p'_1)\right]
$$

$$
\times\int_{x_1}\int_{y_1}e^{i(p_1-p'_1)x_1+i(q_1+p'_1)y_1}e^{-\sqrt{p_{\perp}^2+p_1'^2}|h_{\alpha}(x_1)-h_{\beta}(y_1)+H(\delta_{\alpha2}-\delta_{\beta2})|}. \tag{A12}
$$

This expression will be treated analogous to the case of the matrix for the Dirichlet boundary condition, cf. Eq. (A1). It differs from the Dirichlet kernel by the additional p'_1 dependent term. This yields again Eq. (A5), but now with $N_{\mathrm{D},m}$ substituted by the Neumann matrices $N_{\mathrm{N},m}$, which are given by

$$
N_{\mathrm{N},m}(q_{\perp},q_1) = \begin{pmatrix} A^{\mathrm{N}}_{m,1}(q_{\perp},q_1) & B^{\mathrm{N}}_{m,12}(q_{\perp},q_1) \\ \gamma^m B^{\mathrm{N}}_{m,21}(q_{\perp},q_1) & \gamma^m A^{\mathrm{N}}_{m,2}(q_{\perp},q_1) \end{pmatrix} + \delta_{m0}\begin{pmatrix} -\dfrac{q}{4}(1+e^{-2a_1q}) & \dfrac{q}{2}e^{-qH}\cosh(a_1q)\cosh(a_2q) \\ \dfrac{q}{2}e^{-qH}\cosh(a_1q)\cosh(a_2q) & -\dfrac{q}{4}(1+e^{-2a_2q}) \end{pmatrix} \tag{A13}
$$

for m even, and

$$
N_{\mathrm{N},m}(q_{\perp},q_1) = \begin{pmatrix} 0 & C^{\mathrm{N}}_{m,12}(q_{\perp},q_1) \\ C^{\mathrm{N}}_{m,21}(q_{\perp},q_1) & 0 \end{pmatrix} \tag{A14}
$$

for m odd. The entries are now given by

$$
A^{\mathrm{N}}_{m,\alpha}(q_{\perp},q_1) = \frac{(-1)^{m/2}}{\pi^2}\sum_{k=-\infty}^{\infty}\frac{1}{(m-2k+1)(2k-1)}\frac{1-e^{-2a_{\alpha}\tilde{q}_{2k-1}}}{\tilde{q}_{2k-1}^3}\phi_{mk}(q_{\perp},q_1), \tag{A15}
$$

$$
B^{\mathrm{N}}_{m,\alpha\beta}(q_{\perp},q_1) = 2\frac{(-1)^{m/2}}{\pi^2}\sum_{k=-\infty}^{\infty}\frac{\gamma^{(2k-1)(\delta_{\beta2}-\delta_{\alpha2})}}{(m-2k+1)(2k-1)}\frac{e^{-\tilde{q}_{2k-1}H}}{\tilde{q}_{2k-1}^3}\sinh(a_{\alpha}\tilde{q}_{2k-1})\sinh(a_{\beta}\tilde{q}_{2k-1})\phi_{mk}(q_{\perp},q_1), \tag{A16}
$$

and

$$C^{\mathrm{N}}_{m,\alpha\beta}(q_\perp,q_1) = \frac{(-1)^{(m+1)/2}}{m\pi}\left[(-1)^\alpha\gamma^{m\delta_{\alpha2}}e^{-qH}\left(q+\frac{2\pi m}{\lambda}\frac{q_1}{q}\right)\sinh(a_\alpha q)\cosh(a_\beta q)+(-1)^\beta\gamma^{m\delta_{\beta2}}e^{-\tilde{q}_m H}\right.$$
$$\left.\times\left(\tilde{q}_m-\frac{2\pi m}{\lambda}\frac{q_1+2\pi m/\lambda}{\tilde{q}_m}\right)\sinh(a_\beta\tilde{q}_m)\cosh(a_\alpha\tilde{q}_m)\right],\tag{A17}$$

using the function

$$\phi_{mk}(q_\perp,q_1)=q_1\left(q_1+\frac{2\pi m}{\lambda}\right)\left(q_1+\frac{2\pi}{\lambda}(2k-1)\right)^2+2q_\perp^2\left(q_1+\frac{\pi m}{\lambda}\right)\left(q_1+\frac{2\pi}{\lambda}(2k-1)\right)+q_\perp^4.\tag{A18}$$

As in the case of the Dirichlet matrices, the off-diagonal elements depend on b via the phase factor $\gamma=e^{2\pi ib/\lambda}$. The matrices of the previous discussion of the rectangular corrugation model are now simply recovered by performing the limit $a_2\to0$ and by defining $a=a_1$.

APPENDIX B: THE LIMIT OF SMALL λ FOR THE MATRICES N_m

In this section, the limit $\lambda\to0$ of the matrices $N_m(q_\perp,q_1)$ for the rectangular corrugation model of Sec. III will be performed (cf. Appendix A for $a=a_1$, $a_2=0$, and $\lambda\to0$). These matrices depend on the shift of the argument q_1 relative to $2\pi n/\lambda$, which requires a separate treatment of various cases. Considering this, for the Dirichlet case we find the simplified expressions

$$N_{\mathrm{D},0}(q_\perp,q_1+2\pi n/\lambda)\overset{\lambda\to0}{=}\begin{cases}\begin{pmatrix}\dfrac{e^{-2aq}+1}{4q} & \dfrac{e^{-qH}}{2q}\cosh(aq)\\[2mm]\dfrac{e^{-qH}}{2q}\cosh(aq) & \dfrac{1}{2q}\end{pmatrix} & \text{for }n=0\\[6mm]\begin{pmatrix}-\dfrac{1}{\pi^2 n^2}\dfrac{e^{-2aq}-1}{q} & \epsilon\\[2mm]\epsilon & \dfrac{\lambda}{4\pi|n|}\end{pmatrix} & \text{for }n\text{ odd}\\[6mm]\begin{pmatrix}0 & \epsilon\\[2mm]\epsilon & \dfrac{\lambda}{4\pi|n|}\end{pmatrix} & \text{for }n\text{ even.}\end{cases}\tag{B1}$$

We have introduced a small quantity ϵ, which is needed in order to have a nonsingular matrix B_{kl}. However, at the end we can safely take $\epsilon\to0$ in the final expression for the Casimir force. As $\lambda\to0$, this quantity vanishes as $\epsilon\sim\lambda\exp[-2\pi n(H-a)/\lambda]$. The other matrices for $m\neq0$ are given by

$$N_{\mathrm{D},m}(q_\perp,q_1+2\pi n/\lambda)\overset{\lambda\to0}{=}\begin{cases}\begin{pmatrix}0 & \dfrac{(-1)^{\frac{m-1}{2}}}{\pi m}\dfrac{e^{-qH}}{q}\sinh(aq)\\[2mm]0 & 0\end{pmatrix} & \text{for }n=0\\[6mm]\begin{pmatrix}0 & 0\\[2mm]\dfrac{(-1)^{\frac{m-1}{2}}}{\pi m}\dfrac{e^{-qH}}{q}\sinh(aq) & 0\end{pmatrix} & \text{for }n=-m\\[6mm]\begin{pmatrix}0 & 0\\[2mm]0 & 0\end{pmatrix} & \text{for }n\notin\{-m,0\}\end{cases}\tag{B2}$$

for m odd, and

$$N_{\mathrm{D},m}(q_\perp,q_1+2\pi n/\lambda)\overset{\lambda\to0}{=}\begin{cases}\begin{pmatrix}-\dfrac{(-1)^{m/2}}{\pi^2 n(m+n)}\dfrac{e^{-2aq}-1}{q} & 0\\[2mm]0 & 0\end{pmatrix} & \text{for }n\text{ odd}\\[6mm]\begin{pmatrix}0 & 0\\[2mm]0 & 0\end{pmatrix} & \text{for }n\text{ even}\end{cases}\tag{B3}$$

for even $m\neq0$. Analogously, for the Neumann matrices, we find

$$
N_{\mathrm{N},0}(q_\perp,q_1+2\pi n/\lambda) \overset{\lambda\to0}{=}
\begin{cases}
\begin{pmatrix}
-\dfrac{q}{4}(e^{-2aq}+1) & \dfrac{q}{2}e^{-qH}\cosh(aq)\\[2mm]
\dfrac{q}{2}e^{-qH}\cosh(aq) & -\dfrac{q}{2}
\end{pmatrix} & \text{for } n=0\\[8mm]
\begin{pmatrix}
\dfrac{4(-1)^{n-1}q_1^2}{\lambda^2 q^3}(e^{-2aq}-1) & \epsilon\\[2mm]
\epsilon & -\dfrac{\pi|n|}{\lambda}
\end{pmatrix} & \text{for } n \text{ odd}\\[8mm]
\begin{pmatrix}
-\dfrac{1}{\lambda}\left[\dfrac{\pi|n|}{2}+\dfrac{2}{\pi}\widetilde{C}_0(n)\right] & \epsilon\\[2mm]
\epsilon & -\dfrac{\pi|n|}{\lambda}
\end{pmatrix} & \text{for } n \text{ even}
\end{cases}
\tag{B4}
$$

and

$$
N_{\mathrm{N},m}(q_\perp,q_1+2\pi n/\lambda) \overset{\lambda\to0}{=}
\begin{cases}
\begin{pmatrix}
0 & \dfrac{2(-1)^{\frac{m-1}{2}}q_1}{\lambda}\dfrac{}{q}e^{-qH}\sinh(aq)\\[2mm]
0 & 0
\end{pmatrix} & \text{for } n=0\\[8mm]
\begin{pmatrix}
0 & 0\\[2mm]
-\dfrac{2(-1)^{\frac{m-1}{2}}q_1}{\lambda}\dfrac{}{q}e^{-qH}\sinh(aq) & 0
\end{pmatrix} & \text{for } n=-m\\[8mm]
\begin{pmatrix}
0 & 0\\
0 & 0
\end{pmatrix} \quad \text{for } n \notin \{-m,0\}
\end{cases}
\tag{B5}
$$

for m odd, and

$$
N_{\mathrm{N},m}(q_\perp,q_1+2\pi n/\lambda) \overset{\lambda\to0}{=}
\begin{cases}
\begin{pmatrix}
\dfrac{4(-1)^{m/2}q_1^2}{\lambda^2 q^3}(e^{-2aq}-1) & 0\\[2mm]
0 & 0
\end{pmatrix} & \text{for } n \text{ odd}\\[8mm]
\begin{pmatrix}
-\dfrac{2n(n+m)}{\pi\lambda}\widetilde{C}_m(n) & 0\\[2mm]
0 & 0
\end{pmatrix} & \text{for } n \text{ even},\, n \notin \{-m,0\}\\[8mm]
\begin{pmatrix}
\pm\dfrac{mq_1}{\pi^2}\widetilde{C}_m(n) & 0\\[2mm]
0 & 0
\end{pmatrix} & \text{for } n \in \{-m,0\}
\end{cases}
\tag{B6}
$$

for even $m \neq 0$. Here, the asymptotic behavior of ϵ for $\lambda\to0$ is $\epsilon\sim\lambda^{-1}\exp[-2\pi n(H\pm a)/\lambda]$. The constant is given by $\widetilde{C}_m(n)=(-1)^{m/2}\Sigma'^{\infty}_{l=-\infty}[(2l-1)(2l-1-m)|2l-1+n|]^{-1}$, and the prime at the summation sign indicates that $l \neq (1-n)/2$ if n is odd.

---

[1] H. B. G. Casimir, Proc. K. Ned. Akad. Wet. **51**, 793 (1948).

[2] P. W. Milloni, *The Quantum Vacuum* (Academic Press, New York, 1993).

[3] M. Bordag, U. Mohideen, and V. M. Mostepanenko, Phys. Rep. **353**, 1 (2001).

[4] K. A. Milton, *The Casimir Effect: Physical Manifestations of Zero-Point Energy* (World Scientific, Singapore, 2001).

[5] M. Kardar and R. Golestanian, Rev. Mod. Phys. **71**, 1233 (1999).

[6] J. Israelachvili, *Intermolecular and Surface Forces* (Academic Press, San Diego, 1992).

[7] R. Garcia and M. H. W. Chan, Phys. Rev. Lett. **88**, 086101 (2002).

[8] A. A. Bytsenko, G. Cognola, L. Vanzo, and S. Zerbini, Phys. Rep. **266**, 1 (1996).

[9] K. A. Milton, Phys. Rev. D **22**, 1441 (1980).

[10] K. A. Milton, Phys. Rev. D **22**, 1444 (1980).

[11] S. K. Lamoreaux, Phys. Rev. Lett. **78**, 5 (1997).

[12] U. Mohideen and A. Roy, Phys. Rev. Lett. **81**, 4549 (1998).

[13] H. B. Chan, V. A. Aksyuk, R. N. Kleiman, D. J. Bishop, and F.

Capasso, Science **291**, 1941 (2001).

[14] G. Bressi, G. Carugno, R. Onofrio, and G. Ruoso, Phys. Rev. Lett. **88**, 041804 (2002).

[15] B. Derjaguin, Kolloid-Z. **69**, 155 (1934).

[16] T. Boyer, Phys. Rev. A **9**, 2078 (1974).

[17] D. Iannuzzi, I. Gelfand, M. Lisanti, and F. Capasso, e-print quant-ph/0312043.

[18] G. J. Maclay, Phys. Rev. A **61**, 052110 (2000).

[19] F. M. Serry, D. Walliser, and G. J. Maclay, J. Microelectromech. Syst. **4**, 193 (1995).

[20] A. Roy and U. Mohideen, Phys. Rev. Lett. **82**, 4380 (1999).

[21] F. Chen, U. Mohideen, G. L. Klimchitskaya, and V. M. Mostepanenko, Phys. Rev. Lett. **88**, 101801 (2002).

[22] G. L. Klimchitskaya, S. I. Zanette, and A. O. Caride, Phys. Rev. A **63**, 014101 (2001).

[23] R. Golestanian and M. Kardar, Phys. Rev. Lett. **78**, 3421 (1998).

[24] R. Golestanian and M. Kardar, Phys. Rev. A **58**, 1713 (1998).

[25] T. Emig, A. Hanke, R. Golestanian, and M. Kardar, Phys. Rev. Lett. **87**, 260402 (2001).

[26] T. Emig, A. Hanke, R. Golestanian, and M. Kardar, Phys. Rev. A **67**, 022114 (2003).

[27] R. Balian and B. Duplantier, Ann. Phys. (N.Y.) **112**, 165 (1978).

[28] R. L. Jaffe and A. Scardicchio, Phys. Rev. Lett. **92**, 070402 (2004).

[29] M. Schaden and L. Spruch, Phys. Rev. Lett. **84**, 459 (2000).

[30] H. Li and M. Kardar, Phys. Rev. Lett. **67**, 3275 (1991).

[31] H. Li and M. Kardar, Phys. Rev. A **46**, 6490 (1992).

[32] T. Emig, Europhys. Lett. **62**, 466 (2003).

[33] M. E. Peskin and D. V. Schroeder, *An Introduction to Quantum Field Theory* (Addison-Wesley, Reading, MA, 1995).

[34] J. D. Jackson, *Classical Electrodynamics* (Wiley, New York, 1967).

[35] S. K. Karepanov, M. Y. Novikov, and A. S. Sorin, Nuovo Cimento Soc. Ital. Fis., B **100**, 411 (1987).

[36] G. L. Klimchitskaya and Y. V. Pavlov, Int. J. Mod. Phys. A **11**, 3723 (1996).

[37] V. M. Mostepanenko and N. N. Trunov, Sov. Phys. Usp. **31**, 965 (1988).

[38] H. Gies, K. Langfeld, and L. Moyaerts, J. High Energy Phys. **06**, 018 (2003).

[39] R. Büscher and T. Emig, e-print cond-mat/0308412.